Expanding The IXO Test Setup For The Hard X-ray Imager Integration

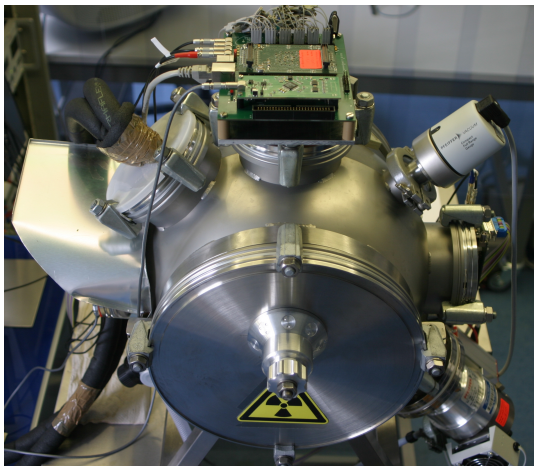

Diploma-Thesis

submitted by
Jurek Loebell

October 2, 2011

Institut für Astronomie und Astrophysik
Eberhard Karls Universität Tübingen

Contents

1 Zusammenfassung **1**

2 Introduction **3**

3 X-ray Astronomy **5**
3.1 X-ray Properties . . . 5
3.1.1 X-ray Generation Processes . . . 5
3.1.2 X-ray-Matter Interactions . . . 9
3.1.3 X-ray Optics . . . 13
3.2 X-ray Sources . . . 14
3.2.1 Stellar Sources . . . 14
3.2.2 Supernova Remnants . . . 15
3.2.3 Pulsars . . . 16
3.2.4 Compact Binary Objects . . . 18
3.2.5 Active Galactic Nuclei . . . 19
3.2.6 Clusters of Galaxies . . . 20
3.3 Historical Overview of X-ray Astronomy . . . 21
3.3.1 UHURU . . . 22
3.3.2 HEAO-1 . . . 22
3.3.3 HEAO-2 . . . 22
3.3.4 ROSAT . . . 23
3.3.5 Chandra . . . 23
3.3.6 XMM-Newton . . . 24

4 Semiconductor Detectors **26**
4.1 Semiconductors . . . 26
4.2 The pn-Junction . . . 27
4.3 Fano Limit . . . 29
4.4 Sidewards Depletion . . . 30
4.5 Charge Coupled Devices . . . 31
4.6 MOS . . . 32
4.7 Fieldeffecttransistors . . . 33
4.7.1 JFET . . . 33
4.7.2 MOSFET . . . 34
4.8 DePMOSFET . . . 36

5 The IXO Mission **39**

5.1 Scientific Goals . . . 39
5.1.1 The Beginning of Structure Formation . . . 39
5.1.2 Evolution of Galaxies and Galaxy Clusters . . . 40
5.1.3 Matter under Extreme Conditions . . . 41
5.2 IXO Optics and Instrumentation . . . 42
5.2.1 The Flight Mirror Assembly . . . 42
5.2.2 Instrumentation . . . 44

6 The Test Setup **51**
6.1 Introduction . . . 51
6.2 The WFI-Detector Prototype . . . 52
6.3 Switcher . . . 53
6.4 The Readout . . . 57
6.4.1 CAMEX . . . 57
6.4.2 Asteroid . . . 59
6.5 The Analog to Digital Converter . . . 60
6.6 The Amplification Stage . . . 61
6.6.1 The S2D-Converter . . . 62
6.6.2 Spice . . . 64
6.6.3 Testing the Amplification Stage . . . 65
6.7 The Event Preprocessor . . . 68
6.7.1 The Framegenerator . . . 73
6.8 The Interface Controller . . . 74
6.9 The Sequencer . . . 75
6.10 IDEF-X . . . 77

7 Summary and Outlook **80**

1 Zusammenfassung

Die Astronomie ist eine der ältesten Wissenschaften. Der Einfluss der Sterne und anderer Himmels Körper auf unser Leben ist in manchen Fällen offensichtlich und allgegenwärtig, wie etwa die Erdanziehung, das Sonnenlicht und die Gezeitenkräfte des Mondes. Aber auch die Strukturentstehungs Prozesse, Nukleosynthese von schweren Elementen und natürlich der Aufbau und die Eigenschaften von Materie haben ihren Einfluss auf unsere Existenz. Astronomie ist ein Schlüsselinstrument für Grundlagenforschung auf diesen Gebieten. Heutzutage wird Astronomie mit Photonen aus dem gesamten elektromagnetischen Spektrum betrieben. Röntgenstrahlung entsteht im allgemeinen bei hochenergetischen elektromagnetischen Wechselwirkungs Prozessen in den Elektronenhüllen von Atomen. Sie kann Informationen enthalten über die Art der Materie, Ionisationsstufen, Temperaturen und Magnetfelder...und damit über die physikalischen Bedingungen in ihrem Entstehungsgebiet. Die hohen Energien von astronomischer Röntgenstrahlung sind verknüpft mit hochenergie Phänomenen des heißen Universums, das eine entscheidende Rolle spielt bei der Entstehung und Entwicklung von Strukturen auf großen Skalen. Mit nur 50 Jahren ist die Röntgenastronomie ein recht junger Wissenschaftszweig der Astronomie, aber die technische Entwicklung über diese Zeit war enorm. Zur Zeit sind vor allem Halbleiterdetektoren die Zugpferde für Röntgendetektion im Energiebereich zwischen 0,1 keV und 15 keV., die eine fast Fano limitierte Energieauflösung bieten zusammen mit hoher Quanteneffizienz.

Das International X-ray Observatory (IXO) sollte eine neue Ära in der Röntgenastronomie einläuten. Es war eine Zusammenarbeit von der National Aeronautics and Space Administration (NASA), der European Space Agency (ESA) und der Japan Aerospace Exploration Agency (JAXA). Ursprünglich planten NASA und ESA ihre eigenen Missionen, Consellation-X und XEUS (X-ray Evolving Universe Spectroscopy). Aber auf Grund von hohen Kosten und großen Überschneidungen, betreffend Instrumente und wissenschaftliche Zielsetzungen, wurden diese beiden Projekte im July 2008 zusammen gelegt zu der gemeinsamen IXO Mission. Allerdings veränderten sich die Rahmenbedingungen, insbesondere bezüglich der NASA Beteiligung und im März 2011 wurde die Umfangreiche IXO Mission reduziert zu der rein europäischen Athena Mission (Advanced Telescope for High ENergy Astrophysics). Diese Diplomarbeit beschäftigt sich mit dem Aufbau einer Testumgebung für den kombinierten Wide Field Imager Hard X-ray Imager (WFI/HXI) Detektor, der eines der Hauptinstrumente von IXO war. Auch wenn sich der Name der Mission geändert hat und in Betreff auf die Instrumente und die Optik Athena ein anderes Design hat, wird sich der Teststand auch weiterhin an den Anforderungen orien-

tiere, die für die wissenschaftlichen Fragestellungen der IXO Mission erforderlich sind. Der WFI/HXI ist ein abbildender Detektor mit hoher Auslesegeschwindigkeit und einem großen Sichtfeld, kombiniert mit einem Detektor für hoch energetische Röntgenstrahlen. Das Ziel dieser Diplomarbeit war es den WFI Teststand auszubauen und für die Integration des HXI vorzubereiten. Der WFI/HXI Detektor bringt für die Röntgenastronomie einige technische Neuerungen, die in Bereichen der Auslesegeschwindigkeit, der Energieauflösung und der Breite des detektierbaren Röntgenbereichs große Fortschritte versprechen. Der Nutzen dieses Teststandes ist die Überprüfung ob die erforderten technischen Ansprüche erfüllt werden können, Erfahrung mit der neuen Technik zu sammeln und die Weiterentwicklung des Detektors.

2 Introduction

Astronomy is one of the oldest sciences. The influence of stars and other celestial bodies on our life in some cases is obvious and omnipresent, like the Earth's gravitation, Sun light and the tides caused by the Moon. However, also the processes of structure formation, nuclear synthesis of heavy elements and of course the structure and properties of matter have their impact on our existence. Astronomy is a key instrument for basic research into these fundamental subjects. Nowadays, the detection methods of astronomy cover the whole electromagnetic spectrum. X-rays originate in general from high energy processes in the electron shells of atoms, covering an energy range between 100 eV and a few hundred keV. They can provide information about the kind of matter, ionisation states and temperatures, and thus about physical conditions in their emission regions. The high energies of cosmic X-rays are related to high energy phenomena of the extreme universe, which plays a major role in the formation and evolution of large scale structures. X-ray astronomy is a very young science with an age of only 50 years, but the technical progress over this period was tremendous. Currently, silicon based semiconductor detectors are one of the working horses for the detection of X-rays, especially in the range between 0.1 keV and 15 keV, where they provide a nearly fano limited (see Section 4.3) energy resolution and high quantum efficiency.

The International X-ray Observatory IXO was planned to start a new era of X-ray astronomy. It was a collaboration of the National Aeronautics and Space Administration (NASA), the European Space Agency (ESA) and the Japan Aerospace Exploration Agency (JAXA). Originally NASA and ESA planned separate missions, Constellation-X and XEUS (X-ray Evolving Universe Spectroscopy). Because of their high costs and large overlaps in terms of instruments and scientific research, in July 2008 these two missions were merged to the joint IXO mission. However, due to budget problems of NASA in March 2011 the ambitious IXO mission was reduced to the European only mission Athena (Advanced Telescope for High ENergy Astrophysics).

This thesis is focussing on the set up of a test environment for the combined Wide Field Imager - Hard X-ray Imager (WFI/HXI) detector, which was one of the main instruments of IXO. Even though Athena has a different design concerning optics and instrumentations, the development test setup will still follow the instrumentation requirements determined by the IXO mission's scientific goals. The WFI is a fast readout, large field of view (FOV) imaging detector, combined with a detector for high energy X-rays. The goal of this thesis was to complete the WFI detector

assembly and prepare it for the implementation of the HXI. The WFI/HXI detector introduces some technical innovations to X-ray astronomy, leading to large improvements in terms of readout speed, energy resolution and the width of the detectable X-ray energy range. The aim of the test setup is to prove, whether the technical requirements can be met, to gain experience with the new technique and to further improve the detectors performance.

3 X-ray Astronomy

3.1 X-ray Properties

X-rays are electromagnetic waves and differ from e. g. optical or radio signals just by their energy range in the electromagnetic spectrum. However, different wavelengths of electromagnetic radiation result in completely different interactions with matter. This section will give a short overview of processes generating X-rays and their matter interactions, in order to prepare the reader for the following chapers.

3.1.1 X-ray Generation Processes

Black Body Radiation

In 1990 Max Planck laid the first foundation to quantum mechanics with his empirical description of Black Body (BB) radiation. Black Bodies are hypothetical physical objects that perfectly absorbe incident photons of all electromagnetic wavelengths. In accordance to Kirhoff's law of thermal radiation, this absorption capability makes them also perfect emitters of electromagnetic radiation. Since a classic calculation of the spectral radiation density inside a BB cavity led to an infinite energy density (UV-catastrophe), Max Planck fitted a measured spectrum with a function, where he had to adapt just one parameter - the Planck constant h. The resulting spectral radiation density is given by

$$U(\nu, T) = \frac{2h\nu^3}{c^3} \frac{1}{e^{\frac{h\nu}{k_\mathrm{B}T}} - 1}$$

where c is the speed of light and $k_\mathrm{B} \approx 8.610^{-5}\,\mathrm{eV/K}$ the Bolzmann constant. The second fraction is the mentioned weighting function introduced by Max Planck. With the beginning of quantum statistics this function turned out to be the density of states for bosons. The electromagnetic wave frequency where a BB has the highest radiation intensity is proportional to its temperature (Wien's displacement law):

$$\nu_\mathrm{max} = \frac{T}{hb}$$

with $b = 2.898 \times 10^{-3}\,\mathrm{m\,K}$ as Wien's constant (Knoll, 1979). Even though BBs are theoretic constructs, spectra of thermally radiating sources are often very similar to ideal bb spectra and additionally have a very characteristic shape. The temperature of a BB radiation emitter that can be seen in X-rays has to be in the range of $10^6 - 10^7\,\mathrm{K}$.

Bremsstrahlung

Bremsstrahlung occurs when charged particles are accelerated in the coulomb field of another charge. Bremsstrahlung is also referred to as free-free interaction due to the unbound state of the accelerated particle before and after the interaction. The spectra of bremsstrahlung cover an energy range up to a cut off frequency determined by the energy of the primary particle. Especially in astrophysics bremsstrahlung occurs predominantly from electron collisions with ions (Schneider, 2006). Bremsstrahlung originating from collisions between two charged particles of the same kind, or more precise of the same mass to charge ratio, is suppressed due to symmetry reasons and the dipole character of the radiation (Rosswog and Brüggen, 2007). For astrophysical sources the most common scenario is a plasma containing electrons with velocities distributed over a broad range. According to Schneider (2006), the emissivity of such a plasma can be described in dependence on its temperature as

$$\epsilon_{\mathrm{ff}} = \frac{32\pi Z^2 e^6 n_{\mathrm{e}} n_{\mathrm{i}}}{3 m_{\mathrm{e}} c^3} \sqrt{\frac{2\pi}{3 k_{\mathrm{B}} m_e T}} e^{-\frac{h\nu}{k_{\mathrm{B}} T}} g_{\mathrm{ff}}(\nu, T)$$

n_{e} and n_{i} are the number densities of electrons and ions in the plasma and g_{ff} is a quantum mechanic correction factor, which is equal to 1 for low temperatures. The bremsstrahlung's spectrum of thermally distributed plasma is rather flat up to a cut off energy as can be seen in Figure 3.1. For astronomical sources also a cut off of the spectrum's low energy part is very likely, due to self-absorption and photoabsorption caused by gas and dust (Schneider, 2006).

Line Emission

Apart from continuum spectra X-rays can also occur in line emission with fixed photon energies. When free electrons or photons of sufficient energy interact with an electron bound in one of the inner shells of an atom, they can ionise the atoms. An electron from a higher energy level can then fill up the resulting unoccupied level, radiating away the energy difference between the two states in form of a photon. The resulting emission line is named after the main quantum number of the lower energy level (K, L, M...), whereas an index indicates the starting state of the transition, beginning at the lowest energy levels (α, β, γ...) (see Figure 3.2). Since

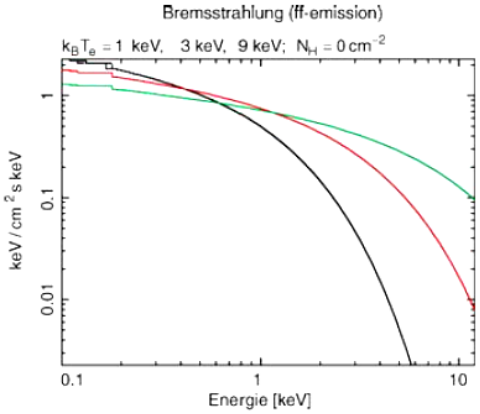

Figure 3.1: Bremsstrahlung spectra of hot gas with three different electron gas temperatures: $k_\mathrm{B}T_\mathrm{e} = 1\,\mathrm{keV}$, $k_\mathrm{B}T_\mathrm{e} = 3\,\mathrm{keV}$, $k_\mathrm{B}T_\mathrm{e} = 9\,\mathrm{keV}$ (Schneider, 2006).

atoms of different elements have different energy levels, line emission provides a clear fingerprint of the emitting atoms. X-rays have energies of more than 100 eV, and are particularly produced at K-series transitions in heavier elements. A distinction is drawn between characteristic radiation and fluorescence, based on the primary ionising particle. Characteristic radiation is said to occur from electrons, whereas ionisation caused by a photon is referred to as fluorescence.

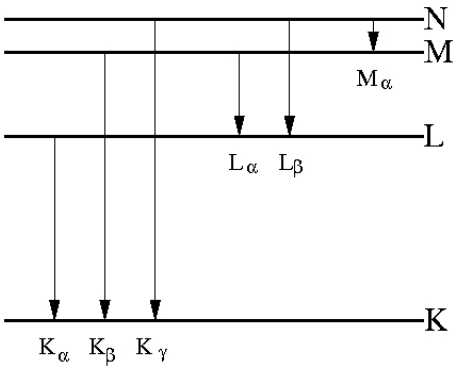

Figure 3.2: Characteristic emission from electron transitions in atomic shells.

Synchrotron and Cyclotron Emission

Synchrotron radiation is produced by relativistic charged particles that spiral around magnetic field lines. Moving on a circular path means permanent acceleration for the particles and therefore they emit electromagnetic radiation. Because of this special generation process, synchrotron radiation is highly polarised. For a uniform

magnetic field polarisation up to 75 % can occur. The synchrotron spectrum of a single electron covers a broad band of energies with a peak near to

$$\nu = \frac{\gamma^2 eB}{4\pi m_\mathrm{e} c}$$

which is one third of the so called characteristic synchrotron frequency (Rosswog and Brüggen, 2007).Cyclotron radiation is principally the same as synchrotron radiation. The difference is just that cyclotron radiation originates from non-relativistic electrons. In astrophysics the probably most prominent example of non relativistic electrons in strong magnetic fields are cyclotron absorption features in the spectra of neutron stars. The hamiltonian of an electron in a magnetic field is given by

$$\mathrm{H} = \frac{(\vec{p} - e\vec{A})^2}{2m_\mathrm{e}}$$

Considering a homogeneous magnetic field, this hamiltonian can be divided into two independent components, the kinetic energy for the motion in direction of the magnetic field and a hamiltonian $\mathrm{H}_\perp$ for the electron motion perpendicular to it. The hamiltonians can be diagonalised simultaneously and have thus the same eigenfunctions. The eigenvalues of $\mathrm{H}_\perp$ are quantised:

$$\mathrm{E}_\perp^\mathrm{n} = \hbar\omega_\mathrm{c}\left(\mathrm{n} + \frac{1}{2}\right)$$

where ω_c is the cyclotron frequency

$$\omega_\mathrm{c} = \frac{eB}{m_\mathrm{e}}$$

On these *Landau levels* the electrons can absorbe photons with certain energies that excite them to one of the next higher Landau levels. The resulting cyclotron absorption features appear e. g. in the vicinity of neutron stars at energies between 10 and 100 keV. They provide the possibility of measuring the magnetic field strenght of neutron stars (Truemper et al., 1978).

Inverse Compton Scattering

Compton scattering is a process where a photon is scattered on a free electron, transferring parts of its energy and momentum. After the interaction the photon energy is given by

$$E' = \frac{E}{1 + \frac{E}{m_e c^2}(1 - \cos\vartheta)}$$

where E is the original photon energy and theta the scattering angle. But in cases of high energy electrons the energy can also be transferred from the electron to the photon. Considering a plasma of electrons and photons, after Rosswog and Brüggen (2007) the net energy transferred by scattering is

$$\left\langle \frac{\Delta E_\gamma}{E_\gamma} \right\rangle \sim \frac{4k_\mathrm{B}T_\mathrm{e} - \bar{E}_\gamma}{m_\mathrm{e}c^2}$$

So for a hot plasma with temperatures higher than $\sim \frac{\bar{E}_\gamma}{4k_\mathrm{B}T_\mathrm{e}}$, photons are upscattered. A prominent example of inverse Compton scattering is the Sunyaev-Zeldovich effect, where photons of the microwave background pass hot gas of galaxy clusters and are inverse Compton scattered to higher energies (Schneider, 2006).

3.1.2 X-ray-Matter Interactions

On the whole there are three dominating kinds of matter interactions for X-rays: the photoelectric effect, Compton scattering and pair creation (Evans, 1955). Each kind of interaction has (depending on the interaction material's atomic number) an energy range where it dominates the others. Figure 3.3 shows the energy ranges where the different processes dominate. All three processes have in common that they are single events, so the photons are scattered or absorbed in just one interaction. The total interaction probability is proportional to the density of the absorber and to its thickness, leading to an exponential absorption law for the intensity of an X-ray beam of a certain energy penetrating an absorber

$$I(x) = I_0\, e^{-\mu x}.$$

The energy dependent linear attenuation coefficient μ is related to the interaction cross section and to the density of the material, and x is the penetration depth. For the selection of a certain absorber material for an X-ray detector, dense solid state absorbers are advisable. They provide high absorption coefficients μ and therefore good quantum efficiencies.

Since X-rays range from 0.1 keV up to about a few hundred keV, interaction processes of X-rays are dominated by the photoelectric effect (see Figure 3.3), where the interaction probability is comparably high. At these wavelengths the Earth's atmosphere is opaque (see Figure 3.5) and no observations of astronomical X-ray sources are possible with terrestrial observatories. For this reason space missions are necessary in X-ray astronomy (see also chapter 3.3).

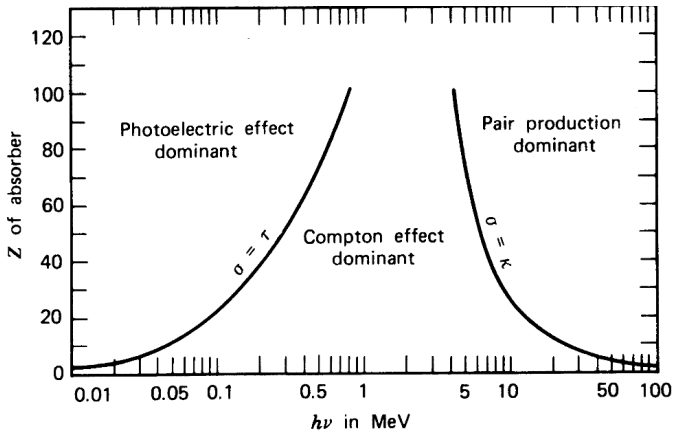

Figure 3.3: The three main different X-ray-matter interaction processes are dependent on the photons energy and the atomic number. The lines divide the atomic number-energy plane into three regions, each dominated by one of the processes (Evans, 1955).

Photoelectric Effect

In the photoelectric effect photons are absorbed in matter by transferring their energy to an electron called photo-electron. Since scattering at free electrons could not conserve energy and momentum simultaneously, this process only occurs as bound-free interaction, which means that the photo-electron is bound first and unbound afterwards. The atomic nucleus or an additional electron has to take a fraction of energy and momentum in order not to violate one of the conservation laws. Also bound-bound processes could be possible like elastic scattering, (anti-) Stokes-Raman scattering, or line absorption however since the depth of electromagnetic potential wells of atoms and X-ray energies are of the same order, the photo-electric effect is by far more likely compared to the bound-bound interactions mentioned above. The energy balance of the photo-electric effect is very simple, but was revolutionary when Albert Einstein interpreted this process for the first time, because that was the discovery of the quantum nature of light. The photon energy is allocated to the electron's kinetic energy and the energy required for the electron to overcome the electromagnetic binding energy $E_\mathrm{b} (< 0\,\mathrm{eV})$.

$$E_\gamma = E_\mathrm{kin} - E_\mathrm{b}$$

The interaction cross section for photo absorption is dependent on the photons energy and on the fifth power of the interaction material's atomic number:

$$\sigma \sim Z^5 \cdot E_\gamma^{-3.5}$$

Therefore, the best absorbers of X-rays are heavy elements like lead ($Z = 82$), whereas beryllium ($Z = 4$) is more or less transparent. For increasing photon energies the interaction cross section drops. However, that is just a general behaviour and invalid when the photon's energy meets the binding energy of the next more strongly bound shell. At those energies additional electrons are available for interactions and the linear attenuation coefficient has a sharp increase. The photoelectric effect dominates X-ray-matter interactions up to energies of $\sim 100\,\mathrm{keV}$ (see Figure 3.3).

Compton Effect

In the region between approximately 100 keV and a few MeV Compton scattering dominates the total photon-matter interaction cross section. Unlike the photo effect Compton scattering is not an absorption process, but the photons are scattered by the electrons. Compton scattering can either be a free-free or a bound-free process, but in the energy range where X-rays are scattered, the electrons can be assumed to be free particles. The energy of the photons after being scattered (as mentioned above) depend on their inertial energy and the scattering angle ϑ

$$E' = \frac{E}{1 + \frac{E}{m_e c^2}(1 - \cos\vartheta)}$$

The differential cross section for Compton scattering is the so called Klein-Nishina cross section σ_{KN} (Evans, 1955), that can be derived from quantum electrodynamics.

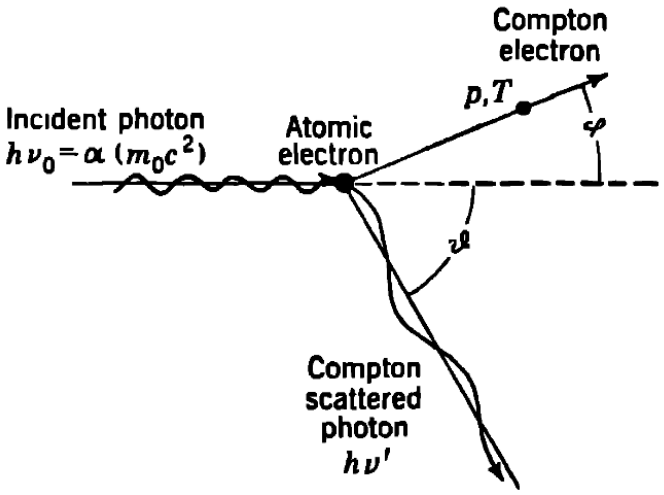

Figure 3.4: Compton scattering: the photon energy $h\nu$ and the scattering angle ϑ uniquely define all other parameters of this process (Evans, 1955).

It describes the angular distribution of scattered photons in dependence on their energy. The total energy transfer cross section can then be calculated by integrating σ_{KN} over all scattering angles.

Pair Creation

When the photon exceeds two times the electron's rest mass energy of 511 keV, pair creation starts to occur. Pair creation means that a photon, interacting in the electromagnetic field of an atom can produce a pair of an electron and a positron. Like any other physical process pair creation has to conserve charge, energy and momentum. Charge conservation is obviously provided and energy can even be conserved when the pair forms in vacuum. But in order to additionally conserve momentum, a collision partner is needed that carries away a fraction of the photons momentum. Therefore, this process only occurs in matter, either with a nucleus as collision partner, or an atomic electron. Of course the energy threshold is higher in the last case, by the binding energy of the electron. The energy of the photon exceeding this threshold is transferred into kinetic energy of the electron, positron and the collision partner.

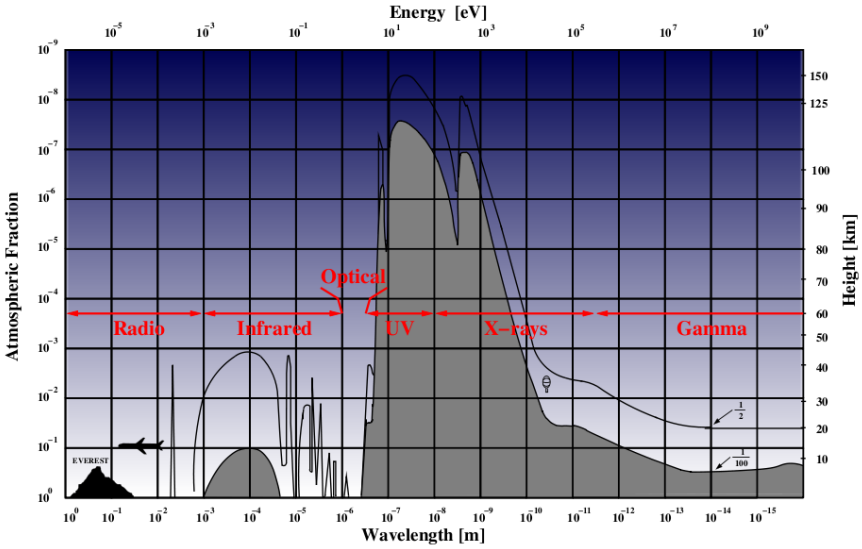

Figure 3.5: The photoabsorption of the Earth's atmosphere. The upper curve shows the altitude, where the radiation's intensity is halved, and the lower curve where only 1 % is left (picture by Giacconi et al. (1968) revised by C. Tenzer and T. Schanz)

3.1.3 X-ray Optics

Besides the penetration capabilities, there is another property of X-rays astronomers have to struggle with. The focussing of X-rays is complicated by the wavelength dependent refraction index (dispersion) of electromagnetic radiation. Since for X-rays vacuum is denser than matter, X-ray photons can only be refracted with gracing incidence using total reflection. There are different possibilities how such gracing incidence optical systems can be realised, but Wolter type I mirror assemblies (see Wolter (1952)) provide the best performance in X-ray focussing and are therefore by far the most widely used optics in X-ray astronomy (Giacconi et al., 1969).

Wolter type I optics consist of two rotationally symmetric mirror shells, a parabolic and a hyperbolic one, aligned behind each other (see Figure 3.6). The focus of the parabolic shell has to be further away from the light source than the focus of the hyperbolic mirror. The system of mirrors allows to nearly satisfy the Abbe sine condition for aberration less focussing. A great advantage of this technique compared to others is that the mirror shells can be nested in order to achieve high effective areas. But as the critical total reflection angle is inversely proportional to the photon energy, only the innermost shells contribute to the effective area for X-rays of higher energies, and the effective area is always smaller for short wavelengths. But apart from using more tightly nested shells, large effective areas for high energy photons can also be achieved by using longer focal lengths.

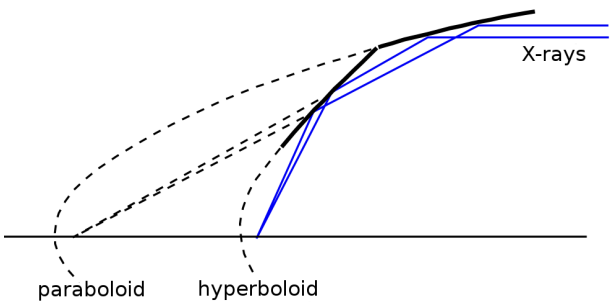

Figure 3.6: The alignment of parabolic and hyperbolic glass shells for a Wolter type I focussing system. The path of incident photons is marked in blue.

3.2 X-ray Sources

The broad range of X-ray generation processes lead to various astronomical sources of X-ray emission. The brightest ones of them will be introduced in the following section.

3.2.1 Stellar Sources

In order to understand the X-ray emission of stars, knowledge about their structure is required. Stars spend the main part of their lifetime on the so called *main sequence* (Unsöld and Baschek, 2002). During that time their inner core consists of a hot plasma ($\sim 10^7$ K (Kippenhahn and Weigert, 1994)), where protons fuse to helium (Longair, 1994b). The core is covered by a couple of shells. Across the convective and the radiative zone, which are the shells next to the core, energy produced in the core is transferred outwards. The radiative zone consists of hydrogen and fusion products. It is stable in the sense that no big plasma bulks move. The energy is transported mainly via radiation. Since the photons are absorbed and emitted again steadily, the light travel time is in the order of 100,000 years (Morison, 2008). The energy transport through the convection zone is much more efficient. Mass movements transport the plasma outwards, where it radiates away parts of its energy before the plasma descends again. The condition required for convection is in particular a steep temperature gradient. In which order the radiative and the convective zone are located depends especially on the mass of the star. Sun like stars have the radiative zone next to the core, whereas the convective zone is located between radiative zone and photosphere. It can be seen through granulations in the photosphere, caused by hotter and cooler regions where hot plasma rises in convective streams and descends when cooled down. In the case of the sun most of the radiation is emitted in form of visible light in the photosphere. The spectrum of these photons looks roughly the same as a thermal spectrum corresponding to a BB of $\sim$ 5800 K temperature (Morison, 2008), so the peak of the emission is at about 2.5 eV. The next shell, the chromosphere, consists of hydrogen and helium with temperatures between 6000 K and 10,000 K (Weigert et al., 2009). Going outwards, the chromosphere merges into the dilute and hot gas of the corona. Usually the corona is not visible, because it is outshone by the photosphere. Only during total eclipses the sun's corona shines against the dark sky (see Figure 3.7).

The corona is a few million Kelvins hot (Rosswog and Brüggen, 2007) and therefore its bulk radiation is emitted in the UV and soft X-ray regime. The heating process that leads to these temperatures is not understood, but magnetic fields seem to play an important role. The magnetic fields of the Sun are very complex and not static. They can form arcs that reach out into space ten thousands of kilometres (see Figure 3.8).

These arcs, or *coronal loops* can store plasma that spirals around the field lines.

From time to time coronal mass ejections occur and the plasma stored in the loops is blown outwards. The mechanism of this effect is unknown, but it is speculated that the field lines, which are twisted because of the differential rotation of the Sun (at the poles the rotation is faster than at the equator) become unstable, tear apart and reconnect again in an untwisted state. The energy set free at this process could drive the mass ejections and accelerate the plasma to velocities of a few thousands of kilometres per second (Hanslmeier, 2011). The frequency of coronal mass ejection occurrence is coupled to the number of sun spots, which are the regions in the photosphere where the magnetic field loops prevent plasma in the convection zone from rising up to the photosphere. Therefore, sun spots are much cooler ($\sim 3700\,\mathrm{K}$ (Unsöld and Baschek, 2002)) than the 5800 K of the photosphere. Since the X-ray emission of the corona is related to the Sun's activity, these magnetic arcs are thought to heat up the corona. X-rays provide the possibility of studying this largely unknown processes in atmospheres of stars, yielding a better understanding of this objects.

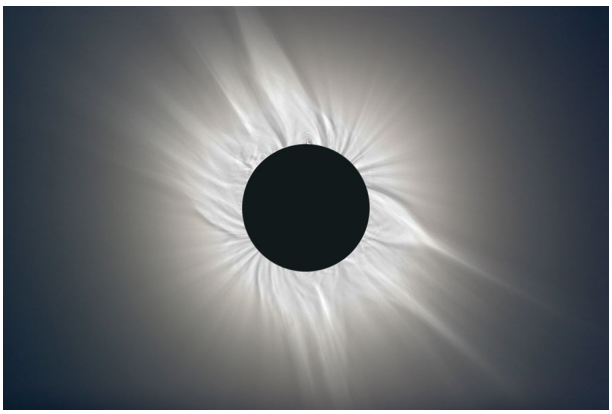

Figure 3.7: The corona of the Sun during a total eclipse (Koen van Gorp).

3.2.2 Supernova Remnants

Supernova remnants (SNRs) consist of ejected matter that expands, driven by a supernova explosion and sweeps up interstellar gas. Supernovae occur mainly due to two reasons. The turning off of nuclear fusion in the innermost core of a star, or suddenly turning it on (Weigert et al., 2009). When massive stars run out of fuel, no radiation pressure prevents the star from collapsing under its own weight. The gravitational energy, which is set free at this process expels and heats up the outer layers. The core of the progenitor star would form either a neutron star or a black

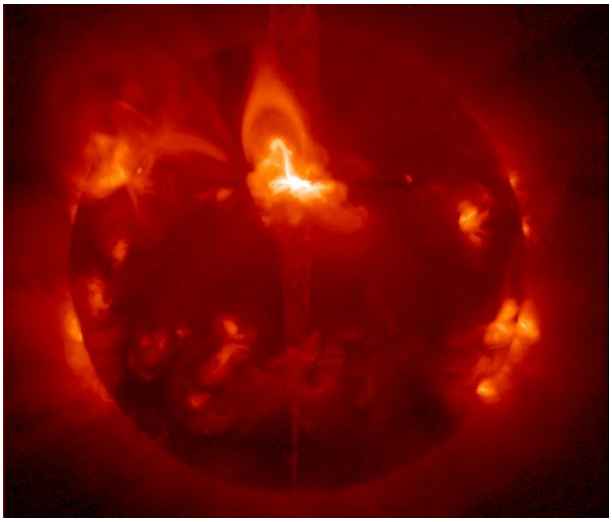

Figure 3.8: Coronal loops of the Sun in soft X-rays (NASA).

hole, depending on its mass. The second scenario occurs in white dwarfs. White dwarfs are corpses of dead stars that don't have enough mass to keep fusion processes in their cores running. But if the white dwarf gets the chance of accumulating gas from a companion star, it can exceed the Chandrasekhar mass of approximately 1.4 sun masses (Chandrasekhar, 1931), which is the maximum mass for a stable white dwarf star. Exceeding this mass would lead to a gravitationally caused core collapse. During the collapse the white dwarfs core heats up until nuclear fusion is triggered. The suddenly released fusion energy disrupts the star, leaving nothing than an expanding cloud of hot gas. SNRs expand with velocities in the order of ten thousands of kilometres per second and can form structures of tens of parsecs extension. They shock the ISM and heat its temperature up to 10^7 K (Longair, 1994b), so it glows in X-rays as e. g. the Chandra observation in Figure 3.9 of the SNR N49 shows.

3.2.3 Pulsars

Pulsars are fast rotating neutron stars. Since all stars have angular momentum and neutron stars form during core collapse of stars (Longair, 1994a), conservation of angular momentum leads to dramatically increased rotation speeds. Rotation periods are normally in the range of 1 - 10 seconds, but also so called millisecond pulsars have been observed (P $\sim$ 1.5 - 30 ms). Not only the angular momentum is affected by the collapse, also the magnetic field experiences an increase when the radius is reduced, due to the conservation of magnetic flux (Longair, 1994a). Pulsars are often assumed to have dipole like magnetic fields. This model can explain many of the observed properties, especially the so called lighthouse effect. When rotation

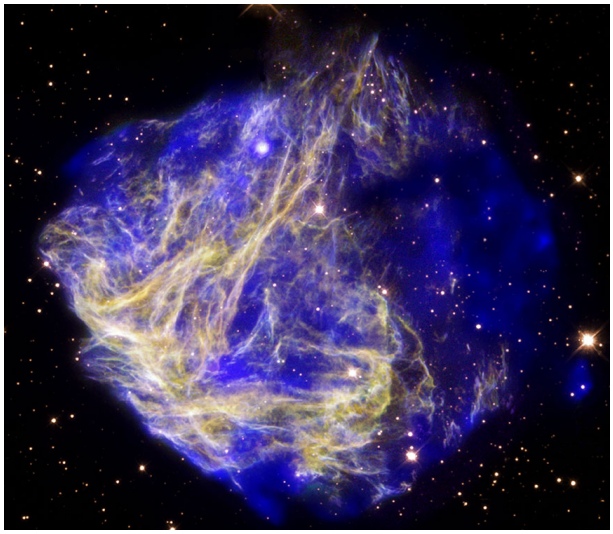

Figure 3.9: False colour image of the SNR N49 in X-rays (blue, Chandra) and visible light (yellow, HST) (NASA)

axis and magnetic field axis are displaced, the magnetic field lines go through the ionised gas in the pulsars atmosphere. Charged particles accelerated in the magnetic field emit synchrotron radiation along the open field lines at the poles as illustrated in Figure 3.10. These photons can reach up to the X-ray regime. When the earth lies within the emission cone's surface, radiation pulses can be detected with the same periodicity as the pulsars rotation.

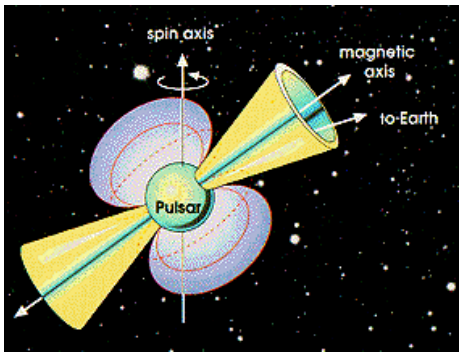

Figure 3.10: A pulsar with misaligned magnetic and rotation axis. X-rays emitted along the open field lines sweep through space in a beam that moves on a cone surface (NASA).

3.2.4 Compact Binary Objects

About half of all stars were found to be part of systems of two or more stars (Unsöld and Baschek, 2002). Two-star-systems containing a compact object like white dwarfs, neutron stars or black holes are called compact binary systems. There are many possible combinations of such systems and they can not all be discussed in this thesis. Therefore, this subsection will concentrate on the most interesting ones in terms of X-ray emission. All X-ray binaries found so far are assumed to harbour either a neutron star, or a black hole and a companion star. The X-ray emission is powered through accretion from the companion onto the compact object. Accretion is the most effective way for energy transformation known so far (Longair, 1994a). Accretion means the process of matter being gravitationally attracted towards a massive object and the thermalisation of the gravitational energy, which is set free at this process into electromagnetic radiation. Considering that a particle accreted from infinity is stopped at a radius R, it has to transfer the kinetic energy it gained during the free fall. This energy is given by

$$E = \frac{1}{2} m v_{\mathrm{ff}}^2 = \frac{GmM}{R}$$

where m and M are the particle's and the compact object's mass and $\mathrm{v_{ff}}$ is the free fall velocity at the radius R. Under the assumption that all energy is transformed into radiative energy and with a mass accretion rate of $\dot{m}$, according to Weigert et al. (2009) this would lead to a luminosity of

$$L = \frac{1}{2} \dot{m} c^2 \left(\frac{R_{\mathrm{s}}}{R} \right) =: \xi \dot{m} c^2$$

where $R_{\mathrm{s}} = 2GM/c^2$ is the Schwarzschild radius of the compact object and ξ is the efficiency of converting gravitational energy into electromagnetic radiation. ξ can be adapted if not all energy is turned into heat. For a neutron star of 15 km radius and a Sun like mass, ξ is approximately 0.1. Just for comparison, in the case of nuclear fission ξ is around 0.001 and for p-p fusion 0.007. For BHs it is more difficult to estimate the energy transfer efficiency, because they don't have solid surfaces and the radius of the last stable orbit depends on the BH spin. General relativity calculations yield $\xi = 0.06$ for spherically symmetric BHs, whereas maximally rotating Kerr BHs can reach values ξ as high as 0.426 (Longair, 1994a).

X-ray binaries are divided in two classes, according to the mass of the companion star. In low mass X-ray binary systems (LMXB) the donor star is a main sequence (hydrogen burning) star of a mass less than 1.4 times the Sun mass, whereas high mass X-ray binary (HMXB) companion stars are young and massive ($> 10 M_{\odot}$). The evolution time scale for massive stars is much shorter than for sun like stars. Therefore, HMXBs are located in the galactic plane, especially in regions of high star formation rates, whereas LMXBs can also be found more close to the galac-

tic poles. Usually, LMXB companion stars have small mass losses through stellar winds. Accretion occurs when the companion star expands and fills up its roche lobe. In this case matter can be transferred through the first Lagrangian point towards the neutron star or black hole. This matter can not be accreted straight onto the compact object because of conservation of angular momentum and is thus orbiting around it, forming an accretion disc. The matter of inner orbits can loose angular momentum via viscous friction until it finally spirals into a black hole or falls onto a neutron stars surface. The accretion stream produces a hot spot where it impacts the accretion disc. Since the gravitational forces are much stronger compared to friction, the disc is assumed to rotate at each radius with its Kepler velocity, leading to differential rotation. Therefore, friction heats up the disc to a few million Kelvin, so thermal spectrum reaches up into the X-ray regime. Additionally X-ray bremsstrahlung can be detected, which is produced when matter is decelerated at the surface of a neutron star (Weigert et al., 2009).

Companion stars of HMXBs are massive and comparably hot and their coronas are very active. They blow out mass on rates of $10^6 - 10^4$ Sun masses per year. Matter that streams towards the compact partner with the right velocity and under the right angle can be accreted (Longair, 1994a). The forming accretion disc is much smaller than for LMXBs, because of smaller angular momentum. However, the mass accretion rates are still high enough for X-ray bright discs (Weigert et al., 2009).

A third type of accretion can occur in X-ray binaries with Be-star companions. The 'B' in the name stands for their spectral class, whereas the 'e' denotes that these stars show emission lines. This emission lines are typically Doppler broadened Balmer series lines. The line's shape reveals that Be stars are fast rotating and due to the high centrifugal forces mass shedding occurs at the equator leading to a disc like atmosphere. If the Be star is part of a binary system with a compact companion, matter of the equatorial disc can be attracted towards the compact partner and form an accretion disc. The generation of X-rays is principally the same as in other binary systems described above, but due to the special conditions it has to be distinguished between three different temporal behaviours of X-ray emission. First, the compact object's accretion disc could touch the equatorial disc at all times, which would lead to constant emission of X-rays. Secondly, X-ray emission with the orbiting periodicity of the system, due to an eccentric orbit. This kind of system is called transient. The third case is caused by sporadic increases in the Be-stars activity, that could trigger the accretion process (Negueruela, 1998).

3.2.5 Active Galactic Nuclei

The luminosity of galaxies is dominated by thermal emission from stars and the intergalactic medium. The temperature of stars varies in the range of a few thousand up to a few ten thousand Kelvin. The spectra of galaxies should thus be composed by Planck spectra, covering an energy range approximately between 1 and 10 eV.

But there are some galaxies that have much broader spectra reaching from radio emission up to X-rays and even gamma radiation. Estimating the luminosities of these sources led to the conclusion, that no stellar sources could be responsible for this emission. They exceed by far ($\sim$ 10,000 times) the luminosity of other galaxies, which are similar in size and the main luminosity is concentrated on a small central region ($\sim 3\,\mathrm{pc}$). Without knowing their nature, the central engines of this emission were named active galactic nuclei (AGN). AGNs were classified by different properties, but as it turned out, they are very likely all the same, at least with concerns to the type of the central engine (Schneider, 2006). Nowadays, a super massive black hole (SMBH) is assumed to be the driving force of the emission, accreting intergalactic gas. The accretion of stars is not very likely, because they carry high angular momentum and can not lose it efficiently enough. A very prominent evidence for a SMBH as central engine is provided by the shape of a 6.35 keV iron K_α line. This fluorescence line is probably emitted at the innermost regions of the AGN's accretion disc. Its profile is affected by the rotation of the disc, relativistic beaming and by gravitational redshift. Therefore, it provides the possibility of putting constraints to the accretor's mass. Accretion discs of AGNs are normally not as hot as in X-ray binaries, so the thermal emission of AGNs is just peaking in the UV-regime. Besides the X-rays emitted in fluorescence lines, AGN X-rays can also originate in the accretion discs corona, where hot gas upscatters photons to X-ray energies via the inverse Compton effect. A big surprise were X-rays emitted in jets, which were only detected by their radio emission before. These jets are highly collimated and highly relativistic matter outflows from the AGN's central region, directed perpendicular to the accretion disc. The underlying mechanism is not known, because the observations can not distinguish between the different models. The most prominent ones are the Blanford-Payne-scenario and the Blanford-Znajek-process (Livio et al., 1999). The X-rays coming from the jet might be produced by so called synchrotron self Comptonization. Radio photons produced in synchrotron emission of relativistic electrons could be upscattered by the electrons to X-ray energies (Schneider, 2006).

3.2.6 Clusters of Galaxies

Clusters of galaxies are after AGN the most luminous extragalactic X-ray sources ($L \sim 10^{43} - 10^{45}\,\mathrm{erg/sec}$). Some clusters contain even more than 1000 galaxies, what makes them the largest structures in universe. The emission region is expanded over scales of $\sim 1\,\mathrm{Mpc}$. The spectral and spatial distribution suggests that the emission originates from a hot gas ($10^7 - 10^8\,\mathrm{K}$), where X-rays are produced via bremsstrahlung. The shape of the resulting spectrum is described in Subsection 3.1.1. Line emission that superimposes the spectra provides an independent possibility of measuring the temperature of the gas. Strongest line is a Lyman α line of 25 times ionised iron (7 keV), that confirms the temperature derived from the spectra's thermal component. This temperature, determined through X-ray emission seems to provide an accurate measure for the viral mass of the cluster. This mass

measurements are important for making assumptions on dark matter constraints and for cosmological research (Schneider, 2006).

3.3 Historical Overview of X-ray Astronomy

In order to understand the technical progress in X-ray detection provided by the IXO mission and the resulting prospects to scientific research, the mission has to be put into a historical context. This section will give a short overview of the history of X-ray astronomy.

The opacity of the Earth's atmosphere for electromagnetic waves in the X-ray regime, delayed the discovery of astronomical X-ray sources to the year 1949. After the second world war, German V2 rockets were brought to the US and used for research purposes. A team of the Naval Research Laboratory led by Herbert Friedmann launched such a rocket with a collection of Geiger-Müller counters aboard and detected X-ray emission from the solar corona. Encouraged by this discovery, Riccardo Giacconi persistently pushed forward to start additional rockets equipped with more sensitive Geiger-Müller counters, to search for astronomical X-ray sources apart from the sun. The first two rocket flights failed, but the third was a success. It was launched with the primary goal to detect solar X-rays reflected at the lunar surface, but instead they found in the constellation of Scorpio a bright source they named Scorpio X-1 (*Sco X-1* for short). For us "earthlings" Sco X-1 is the brightest X-ray source besides the Sun and the first X-ray source to be detected outside of the solar system (Giacconi et al., 1962). This discovery marked the beginning of scientific interest in astronomical X-ray sources and Riccardo Giacconi was awarded with the Nobel Price in physics "for pioneering contributions to astrophysics, which have led to the discovery of cosmic X-ray sources".

In the sixties, various rockets equipped with X-ray detectors were launched. They provided data acquisition times of few minutes, but in order to detect fainter sources, much longer observation periods became necessary. Also balloon based missions were introduced. Balloons make observation times of an order of one week feasible and can carry their instruments to altitudes up to 40 km above sea level. But even in this thin air low energy X-rays are blocked. So to extend the detectable X-ray band towards lower energies and to achieve high observation times, satellites became first choice for X-ray detection. The first satellite missions that found X-ray sources were actually not dedicated for this sources. For example the third Orbiting Solar Observatory (OSO-3), launched in march 1967 was intended to observe solar flares and the four American Vela satellites (5A, 5B, 6A, and 6B) had the primary goal to spot nuclear bomb tests. So the X-ray observations of these missions were only by-products, as these satellites were actually dedicated to different tasks.

3.3.1 UHURU

The first satellite dedicated entirely to cosmic X-ray astronomy was Uhuru. Uhuru was launched on December the 12$^{\text{th}}$ 1970 from a launch site on an old oil platform near the Kenyan coast. The name Uhuru originates from the location of the launch site and the launch day. The 12$^{\text{th}}$ of December 1970 was the 7$^{\text{th}}$ anniversary of the Kenyan independence and Uhuru is the swahili word for freedom. The Uhuru instrumentation comprised two sets of proportional counters mounted back to back, each with an effective area of 0,084 m^2. They were sensitive for 10^{-3} times the Crab Nebula intensity for X-ray photons with energies between 2 and 20 keV. The two sets of counters were collimated by lead plates, provided with drill holes, to different field of views (FOV). One set was optimized for an angular resolution of a few arc minutes squared resulting in a FOV of 0,52°× 0,52°, while the other set had the priority of high sensitivity to isolated sources. Therefore, this set had a much bigger FOV (5,2°× 5,2°), but also a much worse angular resolution of a few tenths of square degree. Uhuru scanned the whole sky and found 339 X-ray sources (Forman et al., 1978) during its three years of life time (for further information about the Uhuru mission see e. g. Giacconi et al. (1971)). Uhuru was followed by many other X-ray missions that obtained more and more detailed X-ray spectra and discovered X-ray bursts and pulsars. Another great step forward was done with the two High Energy Astronomy Observatories (HEAO-1 and 2).

3.3.2 HEAO-1

HEAO-1 was a spinning survey mission. It rotated once per half an hour around its axis, which coincided with the Earth-Sun line. The detectors were orientated perpendicular to this line. This way sources near the galactic poles were observed nearly continuously, whereas sources near the ecliptic were viewed just for a few days per year. Aboard HEAO-1 there were four major instruments, each of them optimized for a special task (Peterson, 1975). Together they covered the energy range from 0.2 keV up to 10 MeV. Besides a comprehensive catalogue of X-ray sources (Wood et al., 1984), HEAO-1 yielded variability studies of various sources down to a time scale of 3 ms and enabled hundreds of optical identifications and source classifications, due to a position accuracy of around one arc minute.

3.3.3 HEAO-2

The HEAO-1 mission was followed by HEAO-2 (which was renamed to “Einstein” after launch), the first imaging X-ray telescope in space. The telescope mainly consisted of a Wolter type I optic and a rotatable instrumentation mount, which was able to put one of four instruments at a time in the focal plane of the flight mirror assembly. The nested mirrors provided an unprecedented sensitivity to faint

sources of 10^7 times the Crab intensity in the energy band of 0.1 - 4 keV, which was several hundred times more sensitive compared to previous missions. Einstein was able to determine source locations with a precision of a few arc seconds and had a FOV of tens of arc minutes squared (Giacconi et al., 1979). The Einstein mission was a milestone in X-ray astronomy. The possibility of resolving extended sources led to numerous discoveries like the X-ray emitting gas in galaxies and clusters of galaxies (Jones et al., 1979; Forman et al., 1979) or X-ray jets aligned with the known radio jets Centaurus A and M87 (Feigelson et al., 1981; Schreier et al., 1982).

3.3.4 ROSAT

The next great step forward in X-ray astronomy that has to be mentioned was the ROSAT mission (ROentgen SATellite). This German, US and British collaboration was launched in June 1990. The satellite harboured two imaging telescopes: the Wide Field Camera (WFC) for extreme ultraviolet radiation (0.04 keV to 0.2 keV) and for photons in the energy range of 0.1 - 2.4 keV the X-ray telescope (XRT), which was a four times nested grazing incident Wolter type I telescope. The latter was used in conjunction either with the Position Sensitive Proportional Counter (PSPC) or the High Resolution Imager (HRI). The PSPC was designed with a large FOV (2°diameter) and moderate spatial resolution ($\sim$ 20 arc seconds). During the first six months, it was exclusively used and performed an all sky survey, that yielded more than 10^5 new sources. For the duration of the following pointing phase, alternating with the PSPC also the HRI was employed to observe selected sources. In contrast to the PSPC it didn't yield spectral resolution, but an angular resolution of $\sim 2''$. Scientific highlights were for example the detection of thermal radiating isolated neutron stars (Treves and Colpi, 1991) and finally, the detection of solar X-rays, reflected at the moon, which had already been the mission goal of Riccardo Giacconis rocket mission in 1962, that instead discovered Sco X-1 (see above).

3.3.5 Chandra

Besides RXTE (Rossi X-Ray Timing Explorer), BeppoSAX, and Suzaku (a Japan satellite), the present working horses of X-ray astronomy are the NASA X-ray flagship telescope Chandra and the ESA mission XMM-Newton, which are currently providing the highest performance with concerns to imaging capabilities and sensitivity to faint sources. Both satellites were launched in the last year of the preceding millennium.

The Chandra optics consist of a four times nested Wolter type I mirror assembly, which achieve the best angular resolution for X-rays between 0.1 and 10 keV so far, due to a mirror surface smoothness of a few atoms and a mirror alignment of unprecedented accuracy. In combination with the High Resolution Camera (HRC), which is one of the two focal plane instruments, the telescope reveals details of

0.5″ extension (Murray et al., 1987). That is equivalent of reading a newspaper at a distance of around 400 meters. The HRC consits of two micro channel plates, aligned behind each other and covering a FOV of 30 arc minutes squared. In order to obtain energy information of incident photons, one of two different grazing spectrometers (one for low and one for high energies) can be flipped into the optical path to diffract the X-rays according to their energy. Either the HRC or the Advanced CCD Imaging Spectrometer (ACIS) can be used to measure the photon position in the focal plane and determine its energy in high accuracy ($E/\Delta E \sim 500$). Whereas the HRC is designed for high spatial resolution, the advantage of using the ACIS is to take X-ray pictures and measure the photon energy at the same time. The ACIS consits of an array of CCDs providing an energy resolution of $E/\Delta E \sim 50$ and frame times of 3.24 seconds. The timing capability is achieved by using the frame store technique, which is described in Section 4.5. To shift all electrons to the frame store area, a shifting time of 41 ms is needed. The shortest possible integration time is coupled to the readout time, which is at least 3.2 seconds. For a further increase of the readout time continuous readout can be chosen. In this mode one dimension in spatial resolution is lost, but whole frame readout times of 2.85 ms become feasible (Nousek et al., 1987). Chandras unique high resolution capabilities combined with high energy resolution, marks another step in the history of X-ray astronomy. The direct comparison of a $\sim$ 200,000 seconds ROSAT exposure of the supernova remnant Cassiopeia-A (see Figure 3.11), with an 2700 seconds Chandra record of the same source demonstrates dramatically the merit of Chandra.

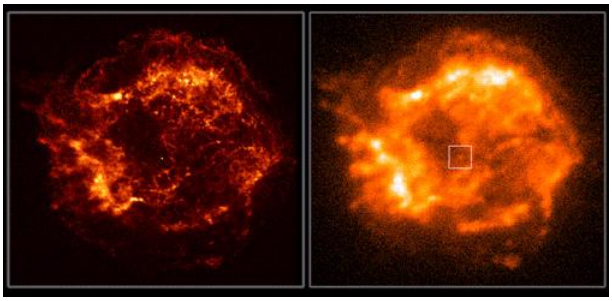

Figure 3.11: Chandra (left) and ROSAT (right) images of the SNR Cassiopeia-A. The resolution difference is tremendous (Weisskopf et al., 2000).

3.3.6 XMM-Newton

The XMM-Newton mission comprises one tube with three telescopes of 7.5 m length, each equipped with 58 nested Wolter type I mirrors and an array of CCDs in the focal plane. The optics provide an unprecedented large effective area of 1500 cm^2 at 1 keV and a moderate angular resolution of five arc seconds. The imaging CCDs are covering a $30' \times 30'$ FOV. They are sensitive for photons up to 15 keV with a spectral

resolution of $E/\Delta E \sim 20-50$ (Turner et al., 2001; Strüder et al., 2001). In order to improve the energy resolution, two of the three tubes are equipped with reflecting grating spectrometers. They deflect about 50 % of the incident photons between 0.3 and 2.5 keV on to additional CCD arrays, each consisting of nine modules. This way energy resolutions of $E/\Delta E \sim 100-500$ are achieved (den Herder et al., 2001). As can be deduced from the instrumentation data, XMM-Newton was designed to detect faint X-ray sources. The FMA is the most sensitive one developed so far. Due to the large FOV combined with moderate angular resolution, good imaging qualities are obtained. Scientific highlights were for example the determination of the mass to radius ratio of neutron stars, enabled by the high sensitivity of XMM-Newton to faint sources (Güver et al., 2010; Özel et al., 2009), that led to constraints to the equation of state of these neutron stars.

4 Semiconductor Detectors

The detection methods for X-rays are manifold and all three matter aggregate states are used as detector material. The advantage of solid state detectors is the high interaction probability, due to a high electron density. Furthermore, using semiconductor devices, good energy resolution becomes feasible, caused by a small pair creation energy (see also Section 4.3). Semiconductors have qualities of both, metal and insulators. They can easily be manipulated to become conductive or isolating and that's why a whole industry uses this kind of matter for various electric applications.

4.1 Semiconductors

If atoms of one kind are put close together in a periodic lattice, the wave functions of their electrons will start to overlap. Therefore, the energy states of degenerate electrons will split up and, in the case of a macroscopic number of atoms, smear out forming energy band structures. By using this energy band model it can easily be differentiated between metals, insulators and semiconductors. In metals the highest occupied energy band is partially filled, whereas in insulators it is completely occupied and there is a big band gap of more than $\sim 5\,\mathrm{eV}$ to the conduction band. Semiconductors have the same band structure as insulators, only the band gap is smaller (for silicon $\sim 1{,}2\,\mathrm{eV}$). Therefore, electrons can be excited to the conduction band by e. g. light absorption or thermal excitation, leaving a hole of an effective positive charge in the valence band (see Figure 4.1) making current flow in both bands possible.

At room temperature the conductivity of pure semiconductors is very low, but it can be modified by replacing atoms of the semiconductor material by atoms of a neighbouring element group. The doping of a 4-valent atom crystal like silicon with atoms of the 5^{th} element group (e. g. arsenic or phosphorus), results in electrons not required for bounding. They occupy energy states inside the band gap, shifting the Fermi energy[1] from the middle of the band gap a bit towards the conduction band. The semiconductor is now called n-doped, due to the majority of negative charge carriers. P-doping for silicon can be achieved by inserting atoms of the 3^{rd} element group (boron, gallium...). Thus unoccupied energy states occur inside the band gap,

[1] The Fermi energy marks the boarder for a certain element between occupied and unoccupied electron states at a temperature of 0 K.

which can be filled with excited electrons from the valence band (see Figure 4.2).

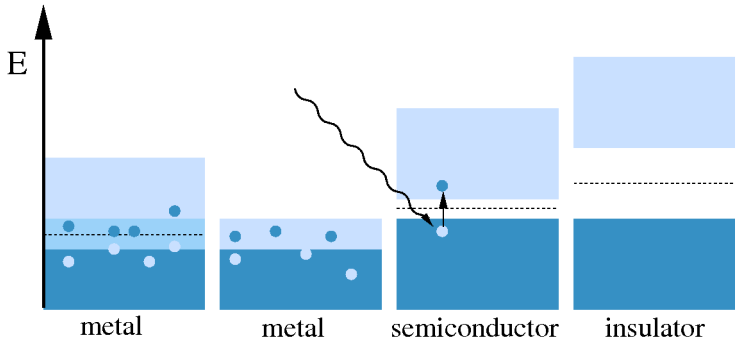

Figure 4.1: Band structure of metal, semiconductor and insulator. Occupied electron states are shown in dark blue and unoccupied in light blue. Due to the small band gap, electrons can easily be excited to the conduction band. The dashed line marks the fermi energy.

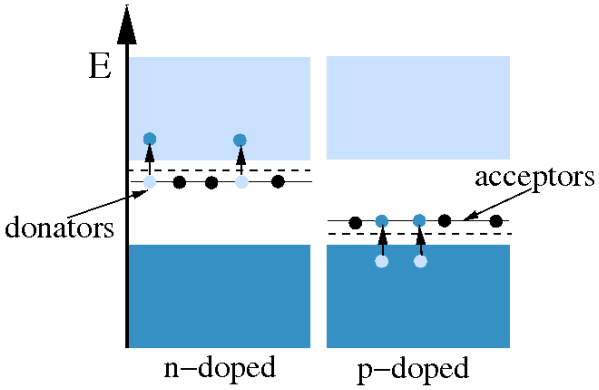

Figure 4.2: Acceptor and donator level of an n- and a p-doped semiconductor. The dashed line marks the fermi energy. In n-doped semiconductors electrons in the donator level can easily be excited to the conduction band, making currentflow possible in both bands. In the case of p-doping, electrons are excited from the valence band to the acceptor level.

4.2 The pn-Junction

The working principle of every semiconductor detector is based on a diode structure. It consists of an n-doped and a p-doped semiconductor. If these semiconductors are

brought together, charge carriers will diffuse across the contact surface, due to a steep concentration gradient of the charge carriers. Electrons (and holes) that enter the p-doped (n-doped) region recombine and cause an electric field directed against the diffusion current. The induced field slows down the diffusion current, until it stops completely. As Figure 4.3 shows, in this state of equilibrium the pn-junction has a charge carrier free, so called depletion zone in the region of the contact surface.

By applying a voltage across the diode, the electric field aforementioned can be increased, decreased or even reversed. In the last, the so called forward biased case (see Figure 4.4), there is nothing to stop the diffusion current and the pn-junction becomes conductive. However, for using semiconductors as detectors, the reverse biased mode is the interesting one. In this configuration a positive voltage has to be applied to the n-doped part of the junction with respect to the p-doped region. Reverse biasing enlarges the depletion zone and the diode gets a high resistance. Even this simple reverse biased diode can be used as X-ray photo detector. Incident X-ray photons deposit their energy via photoelectric effect. The pairs of generated electrons and holes are separated by the electric field, drift apart and recombine at the electrodes. The photon energy can be determined by measuring the amount of current across the juction.

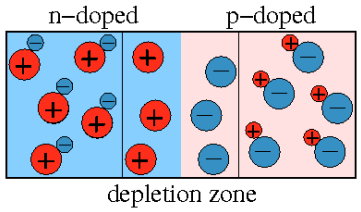

Figure 4.3: pn-junction without externally applied voltages. In the depletion zone between p-doped (pale pink) and n-doped (light blue) region positive and negative majority charge carriers recombine.

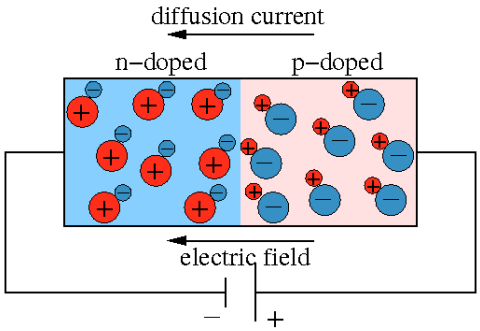

Figure 4.4: Forward biased pn-junction. The depletion zone is surpressed and a current is flowing across the junction.

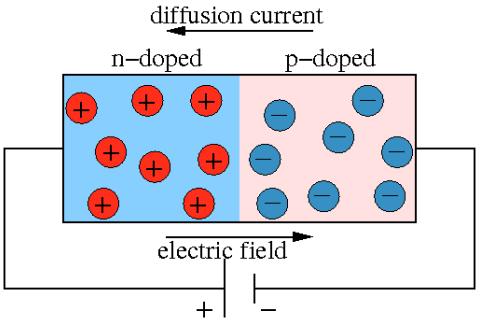

Figure 4.5: Rewerse biased pn-junction. The depletion zone is extended over the whole device. No current flow is possible in this state.

4.3 Fano Limit

Semiconductor radiation detectors have an intrinsic noise, called Fano noise, that limits its theoretical best case scenario energy resolution. Fano noise is caused by number fluctuations of generated electron-hole pairs for photons of the same energy (Fano, 1947). A measure for this fluctuations is the Fano-factor, which is given by the ratio of the experimental number variance and the theoretical one, following poisson statistics. For silicon typical Fano-factors are in the order of 0,1 (Spieler, 2005), depending on purity and doping. This means, that the generation of phonons inside the silicon is not a statistically independent process. For a rough estimate of a fano limited energy resolution, a Fano-factor of 0.1 is assumed at 6 keV

$$F := \frac{\sigma^2_{\text{exp}}}{\sigma^2_{\text{poisson}}} = \frac{\sigma^2}{\langle N \rangle}$$

$$\frac{\Delta E}{E} = \frac{\Delta N}{N} = \frac{2.35 \cdot \sigma}{N} = 2.35\sqrt{\frac{F}{N}}$$

For an average pair creation energy of 3,6 eV in silicon, a 6 keV photon produces $\sim$ 1667 electron-hole pairs

$$\Longrightarrow \Delta E \approx 110\,\text{eV}$$

That corresponds to a number variance of around 13 electrons for a 6 keV photon.

4.4 Sidewards Depletion

For a good signal to noise ratio (SNR) the detector has to have small capacitance (Spieler, 2005), which can be achieved by using sidewards depletion. Sidewards depletion was proposed in 1984 by Emilio Gatti and Pavel Rehak (Gatti and Rehak, 1984). They combined two pn-junctions using an n-doped silicon bulk with two p-doped regions at the bottom side and on top of it. For this device, fully depletion can be achieved with just a quarter of the voltage needed for conventional pn-diodes of the same size, by applying negative voltages to the p-electrodes and a positive voltage to a point-like anode somewhere at the side of the bulk. Figure 4.6 shows how the two depletion zones form and their merging at a certain depletion voltage. At the point where the depletion zones merge, the capacitance between the two p-cathodes and the n-anode drops drastically.

Another advantage of sidewards depletion is the fact, that inside the silicon bulk a potential minimum for electrons forms. In particular this potential minimum can be positioned right below the surface by choosing suitable p-contact voltages (see Figure 4.7). The concept of sidewards depletion is important for nearly all types of charge coupled devices (CCDs) and for silicon drift chambers.

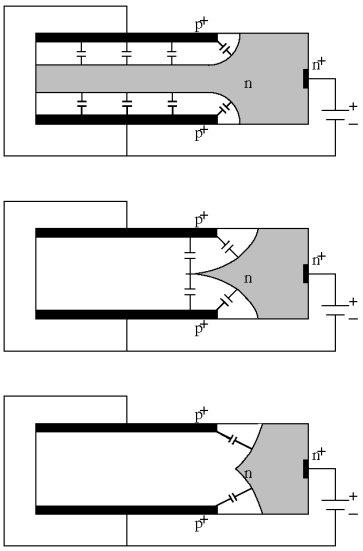

Figure 4.6: The pnp-junction structure used for sidewards depletion. The depletion voltage rises from top down. The white depletion zones grow into the n-doped bulk (grey) and merge at a certain depletion voltage. At this point the capacitance between the electrodes drops drastically.

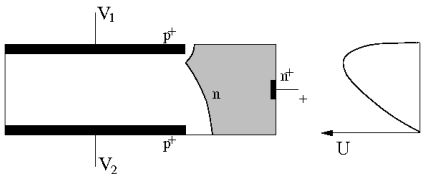

Figure 4.7: In order to create a potential minimum for negative charges inside the semiconductor bulk directly below the surface, the voltage applied to the bottom cathode has to be much more negative than the one applied to the top cathode.

4.5 Charge Coupled Devices

pn-CCD detectors have already been used on board X-ray satellite telescopes (e.g. X-ray Multimirror Mission XMM-Newton) and will be used again on eROSITA (extended ROentgen Survey with an Imaging Telescope Array) of X-ray detection. They are developed on the basis of the aforementioned sidewards depleted double pn-junction structure, proposed by Gatti and Rehak (1984). Due to the shape of the potential, free electrons are stored right below the top electrode, which is fragmented (see Figure 4.8). For a three-phase CCD every third fragment of a column is kept at the same potential. By applying different voltages to the three electrode fragments representing one pixel, a local energy minimum is created below the electrode with the highest potential. The pixels are read out via an anode, located at the end of each column. The charge is transferred from pixel to pixel towards the readout anode by applying periodically changing suitable voltages to the pixel electrodes. For a three phase CCD three voltage pulses called ϕ-pulses are needed to shift the charge from one pixel to another. Apart from three phase CCDs two phase devices are also possible (Beynon and Lamb, 1980).

The readout-time of a whole frame is given by the row shifting time plus row readout time, both multiplied by the number of rows. For faster readout framestore CCDs can be used with twice as much pixels as conventional CCDs, half of them for detection and the other half, which is shielded against radiation, for storing the charges before the readout. With this technique charges can be readout during signal integration and the shifting process is shortened to 115 μs in the case of the eROSITA framestore CCD (Meidinger et al., 2010). Another advantage of this technique is the reduction of out-of-time events, that happen during the shifting process. These events are displaced from their original location by the charge-transfer-speed times the elapsed transfer time.

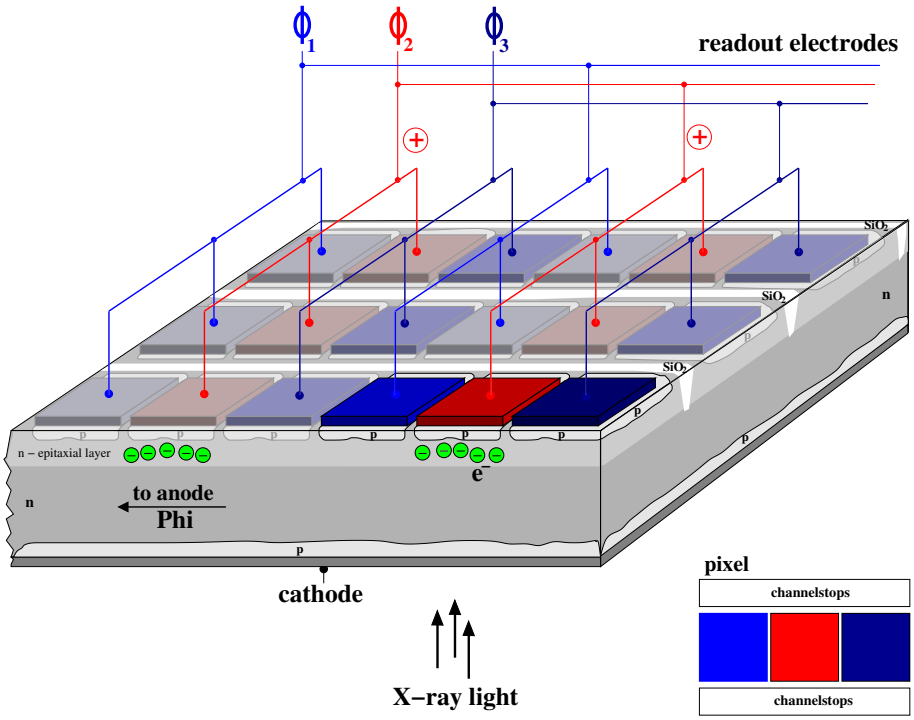

Figure 4.8: The pixel structure of a pn-CCD. Each pixel consists of three electrodes. Free electrons are collected below the electrode with the most positive potential (Thomas Schanz).

4.6 MOS

Besides the pn-junction, there is another very important basic structure for semiconductor devices: the Metal Oxide Semiconductor (MOS). It is a three layer structure of a doped semiconductor, isolated from an electrode, so actually the name should be MIS (Metal Insulator Semiconductor). The name, however, originates from the silicon technology, where silicon-oxide (SiO_2) is used as insulator. Figure 4.9 shows an n-doped MOS with different voltages applied to the electrode. For a positive voltage with respect to the semiconductor, negative charges accumulate next to the insulator layer, while a negative voltage would push away the electrons, forming a space charge region below the electrode. With a negative voltage high enough even an inversion zone can form inside the semiconductor next to the insulator, where then effectively positive charged holes become majority charge carriers. So using a MOS, the charge carrier density inside the bulk can be influenced and that gives rise to a huge number of new applications for semiconductor devices.

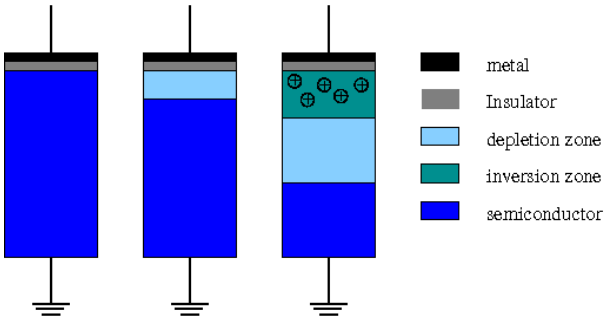

Figure 4.9: The voltage applied to the MOS's cathode drops from the left to the right. At a sufficient negative voltage, positive image charges are created below the cathode.

4.7 Fieldeffecttransistors

There are two kinds of field effect transistors (FET), the junction-FET (JFET) and the MOSFET (metal oxide semiconductor field effect transistor). They are both unipolar, so just one type of charge carriers attend to the transistor current. Bipolar transistors are discussed in detail e. g. in Lutz (1999).

4.7.1 JFET

A JFET consists of two back to back pn-junctions with common n-doped bulk. Figure 4.10 shows an n-channel JFET (for a p-channel JFET doping and all voltages have to be reversed). In operation a voltage is applied across the transistor to the highly doped source and drain, with the drain on a higher potential relative to the source. The result is an electron flow from source to drain. For small source-drain voltages the cross section of the depletion zones at the pn-junctions is nearly constant across the transistor as well as the n-channel, so it behaves like a resistor. By applying a voltage to the p-contacts, the depletion zone can be enlarged or diminished, implicating a higher or lower resistance. At highly negative voltages the transistor is fully depleted and the current flow stops. Therefore, the transistor can be used as a voltage controlled switch. High potential differences between source and drain will cause a cone shaped n-channel, such that the channels cross section will decrease with the distance to the source and can even be "pinched off" at a pinch-off voltage depending on the gate voltage. Since the charge carriers follow the potential drop towards the drain, a current flow is still possible for a pinched off JFET, but the current is only weakly dependent on the source-drain voltage (see Figure 4.11). Thus the transistor is said to be driven in saturation.

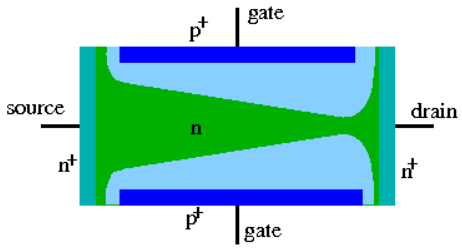

Figure 4.10: The structure of a JFET. The depletion region is marked in light blue. While the gate potentials determine the size of the depletion zones, the source-drain potential difference deforms them.

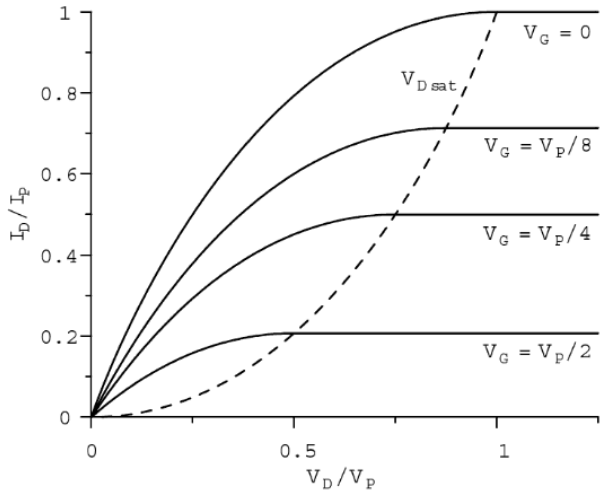

Figure 4.11: Current-voltage characteristic of a JFET in units of the pinch off voltage and the saturation current at the pinch off voltage (Spieler, 2005)

4.7.2 MOSFET

As nearly all semiconductor devices MOSFETs can be used in two configurations, that differ just by interchanged n- and p-doping and reversed biasing. In Figure 4.12 a p-channel MOSFET device is shown. Source and drain are p-doped implementations in an n-doped bulk. The gate consists of a MOS-structure. For a p-channel MOSFET the drain has to be biased negatively with respect to the source. MOSFETs (in contrast to JFETs) can be both, self locking and self conductive. In the first case no current flow is possible between source and drain with an inactive gate, because the two pn-junctions are both reverse biased. But by applying a negative voltage to the gate, positive image charges compensating negative majority charge carriers are generated right below the insulator layer and at a sufficiently negative gate voltage, a channel with positive majority charge carriers forms. So by changing the gate voltage the conductivity of the device can be controlled. A simplified MOSFET source-drain current voltage characteristic is given by Lutz (1999) as

$$I_{\mathrm{D}} = \frac{W}{L}\mu_{\mathrm{p}} C_{\mathrm{ox}} \left[\left(V_{\mathrm{G,eff}} - \frac{V_{\mathrm{D}}}{2} \right) V_{\mathrm{D}} \right]$$

where W and L are the width and the length of the gate, μ_{p} is the charge carrier mobility and C_{ox} is the oxide capacitance per unit area. The effective gate voltage $V_{\mathrm{G,eff}}$ is given by the difference between the actual gate voltage and the threshold gate voltage, where the MOSFET starts to be conductive. This formula is only valid, as long as the drain potential V_{D} is smaller then $V_{\mathrm{G,eff}}$, because for increasing V_{D} the p-channel becomes smaller next to the drain and is finally "pinched off". Although at this point the MOSFET is still conductive (Tietze and Schenk, 2002), I_{D} saturates like shown in Figure 4.13. So for high V_{D} the MOSFET device can be used as constant current source. A very important parameter characterizing a MOSFET is the transconductance g_{m}, which is the partial derivative of I_{D} with respect to the gate voltage:

$$g_{\mathrm{m}} := \frac{\partial I_{\mathrm{D}}}{\partial V_{\mathrm{G}}} = -\frac{W}{L}\mu_{\mathrm{p}} C_{\mathrm{ox}} V_{\mathrm{D}}$$

But again, this is only valid outside the saturation region (see Lutz (1999))

$$g_{\mathrm{m,sat}} := \frac{\partial I_{\mathrm{D,sat}}}{\partial V_{\mathrm{G}}} = -\frac{W}{L}\mu_{\mathrm{p}} C_{\mathrm{ox}} V_{\mathrm{D,sat}}$$

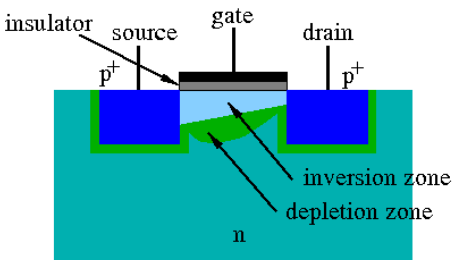

Figure 4.12: The structure of a MOSFET. The gate voltage controls the majority charge carrier density between source and drain and can create a p-channel in the n-doped bulk.

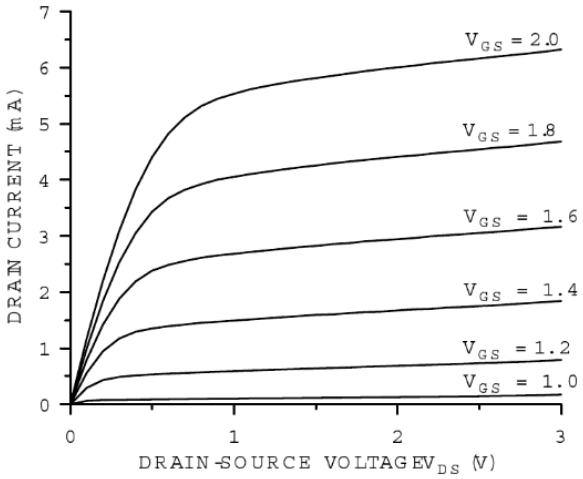

Figure 4.13: A typical current-voltage characteristic of a MOSFET (Spieler, 2005).

4.8 DePMOSFET

The DePFET-detector (or actually DePMOSFET-detector) was first proposed by Kemmer and Lutz (1987) and three years later Kemmer et al. (1990) presented the first experimental results. The pixels of this detector are integrated in an n-doped bulk with a p-doped back cathode. A MOSFET is integrated on top of the semiconductor substrate (Figure 4.14). The detector is fully depleted by sidewards depletion using the back electrode and the p-doped implementations of the MOSFET. Below the gate, which for this device will from now on be referred to as external gate is a deeply n-doped implementation called internal gate. It is very attractive for electrons, so electrons excited to the conduction band by incident photons would drift to the internal gate. The charges stored here effect the p-channel of the MOSFET in the same way a negative voltage applied to the external gate does. So, for a constant current flowing from source to drain and constant drain and gate potentials, the number of electrons inside the internal gate can be determined by measuring the source potential. Apart from this so called source follower readout method, drain current readout can be used as well. This technique requires constant gate and source potentials. The source-drain current is integrated over a fixed time, so that the resulting charge is directly proportional to the charge stored inside the internal gate. Both techniques are non charge destructive readout methods, therefore the pixel has to be reset before the next integration. That is done by a positive voltage pulse to the clear contact (see Figure 4.14). During readout the deeply n-doped clear is sealed of by another MOS-gate (the clear gate). To describe the influence of internal gate charges on the transistor current the charge transconductance g_q is introduced, additionally to the MOSFET transconductance g_m (see also Section 4.7.2). The charge transconductance g_q is the partial derivative of the drain current with respect to the internal gate charges Q_{sig}

$$g_{\mathrm{q}} := \frac{\partial I_{\mathrm{D}}}{\partial Q_{\mathrm{sig}}}$$

Values of $\sim$ 200 - 300 pA/electron have been reported for g_{q} (Treis et al., 2004; Fischer et al., 2003).

DePFET pixel detectors are well suited for imaging. They can be produced with diameters of a few tens of μm and put close together with a filling factor of 100 %. For readout they are contacted in a matrix (see Figure 4.15). Each row has common gate-, clear gate- and clear contacts for all pixels, while the sources are connected column wise (for source follower readout) to the readout ASIC and all drains are brought together to a drainage. The switcher chips are programmed to switch gate, clear gate and clear contact on and off in the right order, to process one row after another, always all pixels of one row in parallel. So the readout ASIC has to have one readout channel for each column. The advantage of DePFET detectors compared to CCDs is due to the small detector capacitance and the signal charge amplification inside the pixel, leading to the name Active Pixel Sensors (APS). Furthermore, the pixels can be addressed directly and the charges don't have to be shifted any more. Therefore, limited charge transfer efficiency and out of time events, which downgrade the performance of CCDs, are ceased and much shorter integration times become feasible.

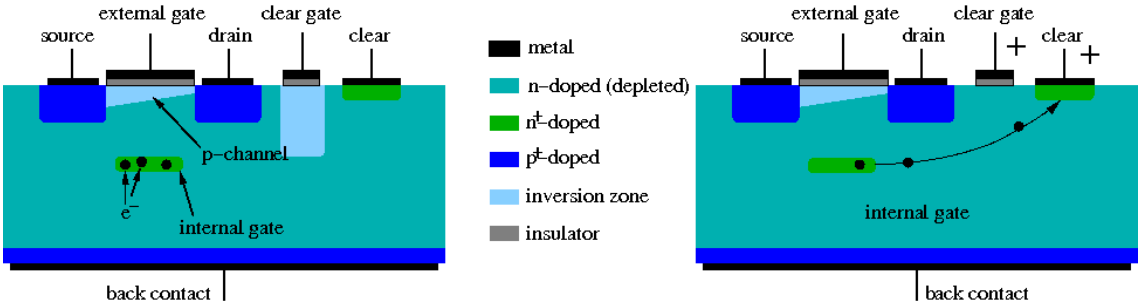

Figure 4.14: A DePFET device in readout mode (left) and during reset (right). Electrones stored inside the internal gate enlarge the p-channels cross-section.

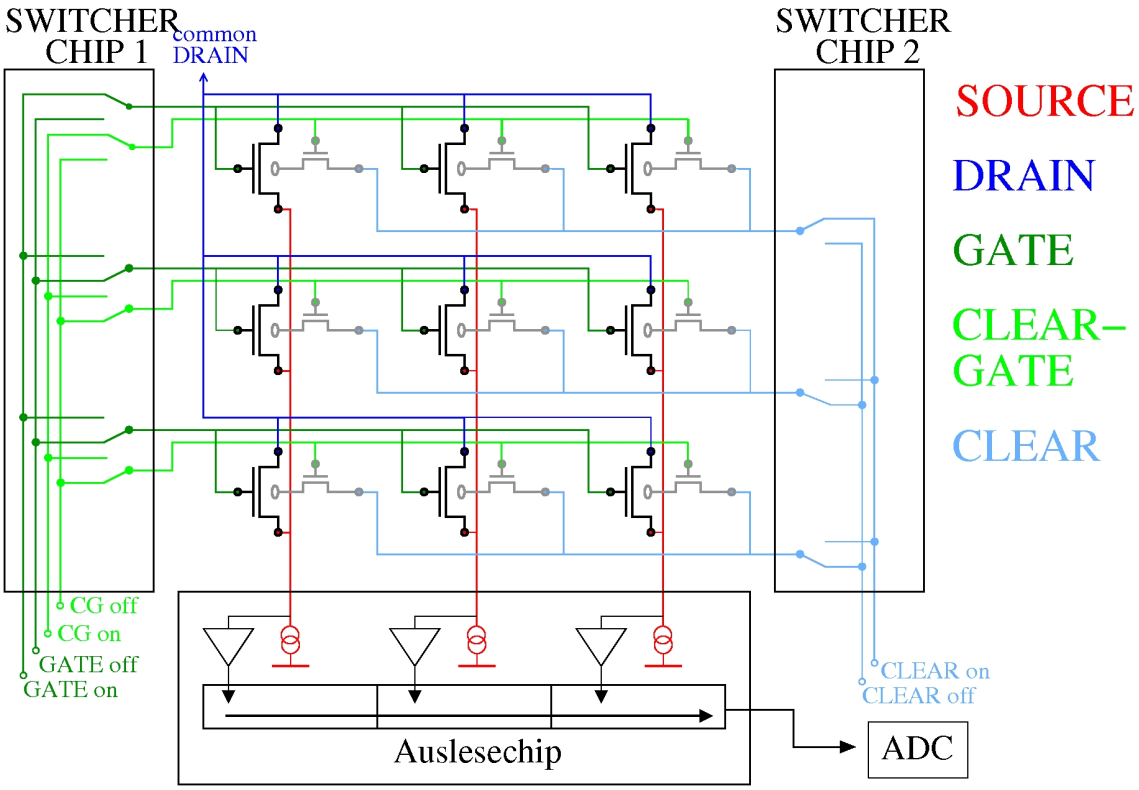

Figure 4.15: 3 × 3 DePFET pixel matrix in source follower readout. The switchers toggle between on and off potentials of the DePFET's readout and reset voltages. Gates, clear gates and clear contacts are connected row wise, whereas all sources of a column are connected to a readout channel of the readout chip (Maier, 2009).

5 The IXO Mission

5.1 Scientific Goals

As mentioned before in the introduction of this thesis, due to changed boundary conditions concerning the participation of NASA and JAXA, the international mission IXO was converted into the European only mission Athena. However, the test setup at the Institute for Astronomy and Astrophysics in Tübingen (IAAT) will still follow the goals of IXO in terms of hardware requirements. Therefore, in this thesis the test setup will be referred to as the IXO WFI test setup, or the IXO WFI/HXI test setup. The following section will treat some scientific goals of the IXO mission, in order to understand the instrumentation requirements and will give an overview of the satellite's payload. IXO would have provided the possibility to study the hot Universe from the very beginning of structure formation, through the evolved large scale structures down to the astronomically smallest scales, where high gravity phenomena occur in the vicinity of BHs and NSs. Where not differently mentioned, this chapter is based on Barcons et al. (2011), Bookbinder (2010) and the references therein. It is structured along three main science topics covered by IXO.

5.1.1 The Beginning of Structure Formation

SMBHs are believed to play a crucial role in structure formation on large scales. The cooling of inter-clusteral medium (ICM) mainly through thermal bremsstrahlung should actually lead to the formation of stars and galaxies in the centre of galaxy clusters on high rates. But there are much less stars and cold gas in the centres of clusters than expected, so there has to be a source that heats the gas, compensating the cooling process. Accreting SMBHs are the number one suspects, but it is still very unclear how this heating works. Studying SMBHs of young age ($z \sim 6$ - 10) could provide information about their role in the formation of large structures. The most efficient way to study them is by using X-ray astronomy. SMBHs of high redshift are likely obscured by inter galactic medium (IGM), but X-rays originating from the innermost orbits of the accreting SMBHs can escape through the surrounding absorbing gas and dust. In order to understand their evolution, SMBHs have to be observed over broad ranges of luminosity, energy, redshift and obscuration. IXO is capable of these observations and with a high spectral resolution and excellent imaging capabilities IXO also provides the possibility to distinguish (up to $z \sim 2$) between winds and jets of outflowing gas and radiative outflows that heat sur-

rounding gas and drive it via radiation pressure. Also star formation itself through supernovae and starburst driven superwinds could account for heating and enrichment of the ICM with heavier elements and therefore retard star formation. There is still very little known about this processes, but high energy resolution direct measurements of gas velocity distributions and turbulences could elucidate the SMBHs' influence on structure formation. Some theories suggest, that SMBHs have a strong growth phase during a period of high obscuration. A good indicator of SMBHs' growth mode is their spin. SMBHs that gain most of their mass by merging are frequently fast spinning, whereas small fragment accretion favours low spins (Berti and Volonteri, 2008). Therefore, IXO is designed to provides a large effective area at 6 keV to determine the SMBH spins via their iron K_α line profile.

5.1.2 Evolution of Galaxies and Galaxy Clusters

The evolution of galaxies depends on the physical and chemical properties of the IGM, which in turn is effected by energy outflows of AGN and metal enrichment. Currently the studies of galaxies and their gas is limited to the nearby universe ($z < 0.5$), but with its unprecedented sensitivity and spectral resolution IXO will extend this observations to redshifts of $z \sim 2$, where the first low mass clusters occurred. The comparison of different age clusters and their properties will elucidate the production mechanisms of heavy elements in galaxies and their ejection in the ICM. Also cosmological findings can be derived from observations of galaxy clusters, due to an independent measurement of redshift and distance. The latter will be determined through the X-ray emitting gas mass fraction (Allen et al., 2004, 2008). IXO will observe hundreds of clusters in the redshift range $0.5 < z < 2$ in order to constrain the redshift to distance relation and thus the amount of dark energy.

Another question that can be answered by IXO is the mystery of missing baryons. Only 10 % of the baryonic matter lies in collapsed objects like galaxies, stars or cold gas. Some of the missing baryons were found to be warm gas (Danforth and Shull, 2008). The warm baryons were detected by absorption features of starlight (at redshifts of $z \leq 0.4$) that travelled through intergalactic warm gas. This gas was ionised by photo ionisation (reionisation) probably in the region of $z \sim 17$, as can be derived from WMAP data. But for sources of higher redshift ($z \leq 0.4$), the lines of the Lyman alpha forest start to overlap and can't be distinguished any more. So warm gas beyond redshifts of $z = 0.4$ could account for an additional fraction of baryonic matter, but there are still 30 % - 50 % missing. This missing baryons could be represented as hot gas. Simulations of structure formation predict that these baryons were shock heated to temperatures up to 10^7 K (Kang et al., 2005) by shock waves that result when large structures collapse in dark matter potential wells. These hot baryons can only be observed through X-ray absorption features against the background of bright AGN. But the current missions Chandra and XMM-Newton do not provide sufficient throughput and spectral resolution to clearly identify their signature.

5.1.3 Matter under Extreme Conditions

The most efficient way of energy transformation so far known is by accretion. Matter orbiting a BH is exposed to high gravitational forces. X-rays emitted by this matter carry information about the extreme conditions in the BHs' vicinity, which are responsible for the accretion mechanism and for particle acceleration in relativistic jets. In order to study these objects and their accretion rates, fast readout is required to resolve suborbital time scales and a large effective area at 6 keV is necessary to examine the spectral profile and determine the BH spin via the shape of the Iron K_α line. Spin determination can also be performed by measuring the polarization of photons emitted from close to the Schwarzschild radius. Their plane of polarization is rotated by an amount depending on the curvature of the space time and its torsion (frame dragging), which is caused by the BH's spin.

Also neutron stars can be observed through X-ray emission. They are the objects with the highest observed densities in the universe. The general behaviour of nature, that matter under extreme conditions decays into its subcomponents, makes neutron stars interesting objects to study. It is still very little known about the composition of their cores. Different scenarios have to be taken into consideration. At a few times the density of atomic nuclei, baryons could appear differently than as neutrons or protons. The core density might even be high enough for baryons to dissolve to quark matter. In this case the inner core of a neutron star could consist of strange quark matter, which is speculated to be the absolute ground state of the strong interaction force. Different behaviours of baryonic matter under the extreme pressure in the cores of neutron stars are reflected in different pressure-density relations (also referred to as *equations of state*). The equation of state (EOS) in turn, leads to different relations of macroscopic measurands such as the mass-radius relation, which in cases of spherical objects can be derived from the Tolman-Oppenheimer-Volkov (TOV) equations (see Oppenheimer and Volkoff (1939)):

$$\frac{dP(r)}{dr} = -\frac{G}{r^2}\left[\rho(r) + \frac{P(r)}{c^2}\right]\left[M(r) + 4\pi r^3 \frac{P(r)}{r^2}\right]\left[1 - \frac{2GM(r)}{c^2 r}\right]^{-1}$$

$$\frac{dm(r)}{dr} = 4\pi\rho(r)r^2$$

So the mass-radius relation seems to be a good probe of the conditions inside neutron stars. One way to determine the mass-radius relation of a neutron star is to use waveform fitting on X-ray burst oscillations. This oscillations are probably caused by the emission from a hot spot on the neutron star surface. The rotation leads to a luminosity oscillation, which is effected by Doppler boosting and by relativistic and gravitational light bending. Waveform fitting of these oscillations could yield constraints on the space-time around the neutron star and simultaneously on its mass and radius. In order to detect these oscillations, high photon throughput and high time resolution are required.

There are actually much more questions IXO might answer (Barcons et al., 2011). But the tasks mentioned above are exemplary in terms of instrumentation requirements. The IXO telescope was planned to be equipped with six different instruments and a focussing optics that can achieve the scientific goals, which are also summarized in in Table 5.1, together with the respective instruments that will be introduced in the next section.

5.2 IXO Optics and Instrumentation

5.2.1 The Flight Mirror Assembly

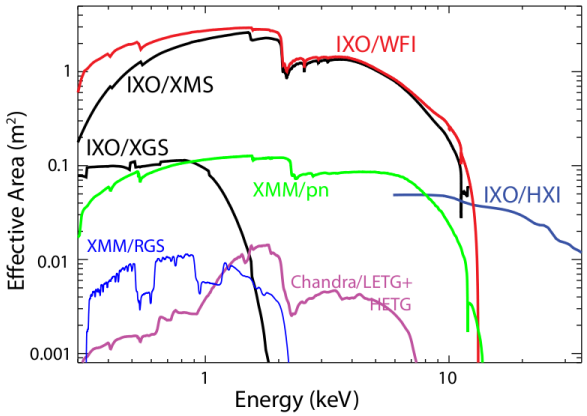

Figure 5.1: Effective areas of IXO, Chandra and XMM-Newton for their different instruments. IXO would have provided a much higher sensitivity to faint sources over the whole energy range (Bookbinder, 2010).

The IXO Flight Mirror Assembly (FMA) was planned to be a Wolter type I optics with an effective area of 3 m^2 at 1.25 keV, 0.65 m^2 at 6 keV and 150 cm^2 at 30 keV. The large effective area at high energies can only be achieved with a focal length of 20 m enabled by an extendable optical bench. The angular resolution requirements are 4 arc seconds below 7 keV and 30 arc seconds at 30 keV. Especially the large effective area is a great improvement compared to previous missions like Chandra and XMM-Newton, as can be seen in Figure 5.1. In order to achieve this ambitious goal, a large number of nested mirrors is needed with a low mass to effective area ratio, to stay within the launch rocket mass constraints. Two different techniques were developed in parallel to reduce the risk of not meeting the FMA performance requirements in time. The baseline technology for the IXO FMA was silicon pore optics (SPO). The advantage of SPO is the low mass to effective are ratio in comparison with segmented glass optics (SGO), which is the backup technique for the

telescope. Furthermore, the SPO mirrors are very robust and stiff, providing angular resolution on the arc second level. But in contrast to conventional X-ray focussing techniques SPO mirrors have to be interlinked by integrated ribs (see Figure 5.2) that reduce the effective area. The mirrors are coated with iridium providing high reflectivity in the X-ray regime. In order to achieve an angular resolution of 4 arc seconds the two stacks of mirrors required for the Wolter optics have to be aligned relatively to each other with at least micron precision. Figure 5.2 shows one test petal of the IXO FMA. Each petal consists of blocks of SPO and these blocks in turn consist of hundreds of silicon plates.

The SGO backup plan for the FMA comprises 349 nested glass shells, each of them thermally brought into the required shape using the slumped glass technique. This technique is schematically shown in Figure 5.3. A sheet of glass is put on a mold, which is individually shaped for each glass segment. The glass sheet softens when heated up to a temperature of around 600 °C and wraps itself around the mold, replicating the mold's surface. Unlike the SPO stacks, the glass segments are not very stiff and can deform under their own weight or when not properly mounted. The mounting and alignment of the segments are the work steps that still provide room for improvement (Barcons et al., 2011).

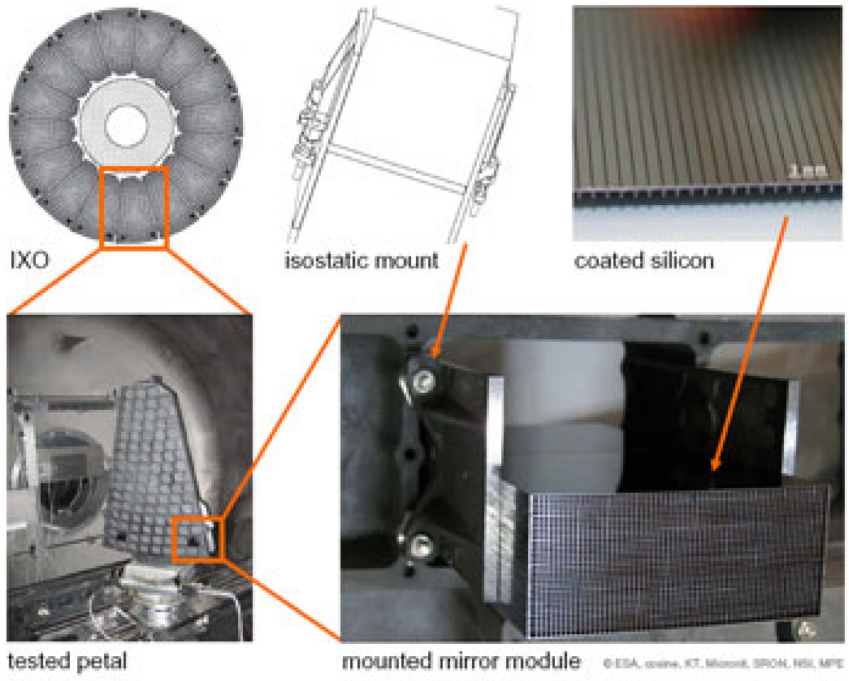

Figure 5.2: The IXO FMA is subdivided into petals (left), each consisting of SPO layer blocks (right) (NASA, 2010).

Figure 5.3: Forming an SGO sheet. When heated up to a temperature of about 600℃ the glass sheet softens and wraps itself around the mold (Barcons et al., 2011).

5.2.2 Instrumentation

Five of the six IXO instruments are mounted on a moveable platform in the focal plane of the telescope. By rotating this platform, one of the instruments (or two in the case of the WFI/HXI) can be put into the focus. Only the camera for the X-ray grating spectrometer (XGS) is a fixed instrument. It can work simultaneously to the other instruments, due to a different beam path (see Section 5.2.2 and Figure 5.4).

X-ray Grating Spectrometer

The XGS is an instrument dedicated to a high energy resolution of $E/\Delta E \sim 3000$ according to (Barcons et al., 2011) with an effective area of $1000\,\mathrm{cm}^2$ across its operating energy range of 0.3 - 1 keV. With these properties, the XGS can be used to determine the chemical composition of the warm and hot intergalactic medium and solve the mystery of the missing baryons. The XGS consists of two components. A set of wavelength dispersive diffraction gratings, placed in the X-ray beam between the optics and the focal plane instruments and a series of CCD detectors. The gratings have a fine pitch ($>$ 5000 lines/mm) to disperse some of the X-ray photons to the CCDs. There were two different geometric solutions for the XGS worth to consider. The critical angle transmission gratings (CAT) and an off-plane reflection grating (OP-XGS). It has not yet become clear which technique provides the better performance (Barcons et al., 2011). The different geometric concepts can be derived from Figure 5.4.

X-POL

The X-ray polarimeter X-POL is a detector with sensitivity to polarisation in the energy range of 2 - 10 keV and also imaging capabilities ($2.6' \times 2.6'$ FOV and $5''$ angular resolution). It is based on a gas pixel detector. Photons pass a thin beryllium entrance window and deposit their energy by generating a photo electron in a 1 cm absorption gap. This photo electron will ionize atoms along its path. An

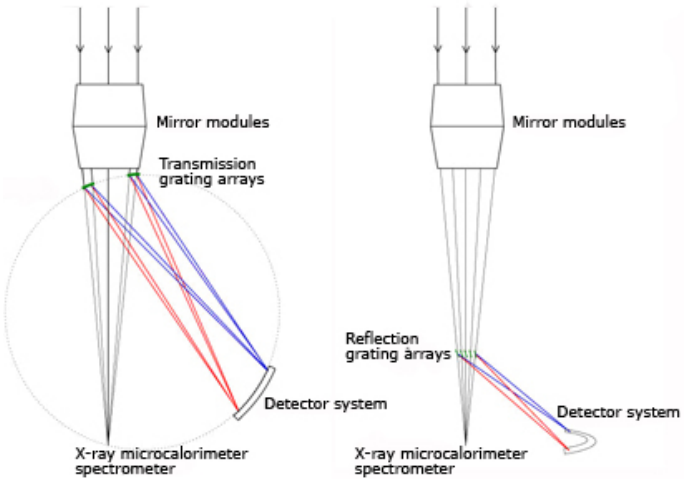

Figure 5.4: The IXO XGS geometry. CAT (left) and OP-XGS (right). Wavelength dispersive diffraction gratings diffract photons out of the X-ray beam towards an array of CCDs (NASA, 2010).

electric field will accelerate the secondary electrons to a $15 \times 15\,\mathrm{mm}^2$ sensitive area covered by a multi channel plate. Each multiplier channel is provided with one of 105600 hexagonal pixels and a readout chain. Since the direction of the photo electron emission is correlated to the X-ray polarization by a $\cos^2(\phi)$ law, the X-ray polarization can be derived with sufficient statistics from the two-dimensional image of the track. The readout ASIC has an auto triggering system, so only the region of interest is read out, saving a factor 100 in readout time. For reconstructing the track, an algorithm identifies the starting point of the track, calculates the photo electron's direction of emission and determines the photon energy with a precision of $E/\Delta E \sim 5$. The photon energy is proportional to the number of electrons generated along the photo electron path (Barcons et al., 2011).

High Time Resolution Spectrometer

In order to probe accretion in the vicinity of BHs and NSs, high count rate capabilities are required together with moderate spatial resolution. The IXO HTRS meets these requirements with an energy resolution of 150 eV at 6 keV simultaneously with 10 µs time resolution and a low dead time. The HTRS comprises 31 silicon drift detector macropixels (SDD, see Figure 5.6), which are very similar to DePMOSFET pixels - only the readout is different (see Figure 5.5).

Suitably biased drift rings drive the electrons generated by incident photons towards a readout anode in the centre of the pixel. The readout anode is connected to the gate of an integrated JFET. SDDs provide an even lower detector capacitance in

comparison with DePMOSFET pixels and therefore a lower electronic noise, but they are almost exclusively used in time continuous readout. In this configuration each pixel has its own triggering electronics, so they can't be connected in a matrix. In order to observe also the brightest X-ray sources, the sensor will be placed slightly out of focus, to spread the photons over the whole detector, avoiding pile up and out of time events. These events make up less than 2 % at a count rate of 1 Crab for the HTRS (Barcons et al., 2011).

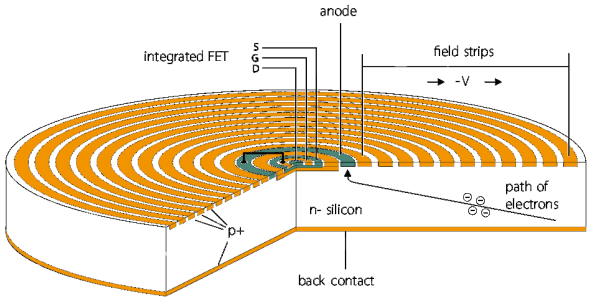

Figure 5.5: Silicon drift detector macropixel. The driftrings on top of the device form a cone shaped potential inside the bulk and drive free electrons to the readout component in the centre of the pixel (MPI Halbleiterlabor, Neuperlach).

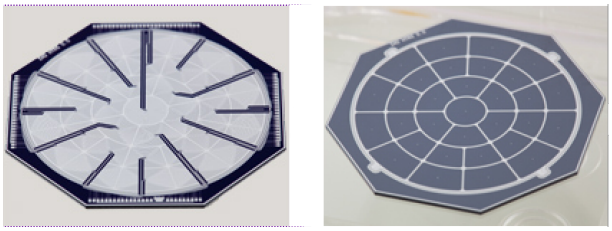

Figure 5.6: The IXO High Time Resolution Spectrometer (frontside, left and backside, right) consists of 31 macropixels, each with its own triggering and readout system (MPI Halbleiterlabor, Neuperlach).

X-ray Microcalorimeter Spectrometer

The IXO XMS provides very high spectral resolution over a broad energy range (0.3 - 12 keV) and simultaneously moderate imaging capabilities. The operating principle of the calorimeter is illustrated in Figure 5.7. An incident photon will deposit its energy in the absorber material, causing an increase of the temperature. The

absorber has a strong thermal link to a sensor, which is kept at its phase transition temperature between a conducting and a superconducting state. The detection of a photon would lead to an increase of the sensors resistance, proportional to the photon energy. A weak thermal contact links the sensor to a heat sink, that cools down the sensor back to its operating temperature. In order to meet the required 5 × 5 arc minutes FOV with a realistic amount of pixels, two different pixel types are used. 1600 pixels arranged in a squared inner array provide an unprecedented energy resolution of less than 2.5 eV at 7 keV. They cover a 2 × 2 arcminutes FOV with a pixel size of 300 µm squared. The pixels in the outer array are 4 times larger and also the energy resolution is about 4 times worse. They complete the sensitive area to the 5 × 5 arc minutes FOV. The operating temperature at 50 mK is a great challenge for use in space applications. The cooling system is split into two components. The primary cooling chain uses Stirling coolers and a Joule-Thompson cooler. This cooling stage attains a temperature of 4 K. The last cooling stage takes advantage of the magneto-caloric effect, using a 3-stage demagnetisation refrigerator. This last stage enables the operating temperature of 50 mK.

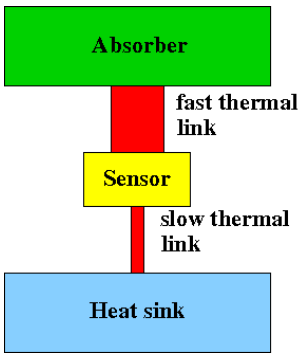

Figure 5.7: Operation principle of an XMS-pixel. The sensor is kept at its conductive-superconductive transition temperature. An absorbed photon would lead to an increase of the sensor's resistance, that can be measured. The heat sink cools the sensor down again to its operating temperature of 50 mK.

The Wide Field Imager

The effective area of IXO in the energy band from 0.1 keV up to 15 keV is much larger than for previous missions (see Figure 5.2). In order to provide a large FOV imaging detector, the resulting instrument requirement is a very high readout rate. DePFET pixels are highly suited for this task. The operating principle of these pixels is described in Section 4.8. The WFI matrix covers a FOV of 18 arc minutes diameter. As the FMA does not only focus X-rays, but also optical light and electromagnetic waves in the ultra violet regime, this radiation has to be blocked to

avoid high optical and UV photon loads. The optical blocking filter consists of a thin aluminium layer, whereas the UV blocker is foreseen to be a silicon oxide/nitride multi layer. In order to ensure that the angular resolution is limited by the FMA and not by the detectors pixel size, a roughly five times oversampling is foreseen, requiring a 100 µm × 100 µm pixel size. That determines the number of pixels to be 1024 × 1024 to cover the whole FOV. Figure 5.8 shows the WFI silicon wafer. To achieve the required high readout speed, the detector is subdivided into two hemispheres. The hemispheres in turn consist of eight areas, readout by their own readout ASIC. So each ASIC is responsible for 128 × 512 pixels. Based on the readout line speed of the foreseen Asteroid ASIC (see also Section 6.4.2) and a 14 bit energy encoding by an ADC, the WFI would produce data rates in the order of gigabits per second, making a very efficient on board data reduction necessary (see Section 6.7).

With these six instruments IXO covers the whole range of its scientific goals. For all instruments, except the HTRS and XPOL, there is even a backup instrument as can be seen in Table 5.1, that allows to address the same science goal. The data of this table is extracted from IXO Bookbinder (2010). It summarizes the scientific objectives, their technical requirements and the corresponding instruments. Some of the instrument requirements are marked with an N/A (not available), indicating, that this individual requirement can not be met within the IXO mission concept.

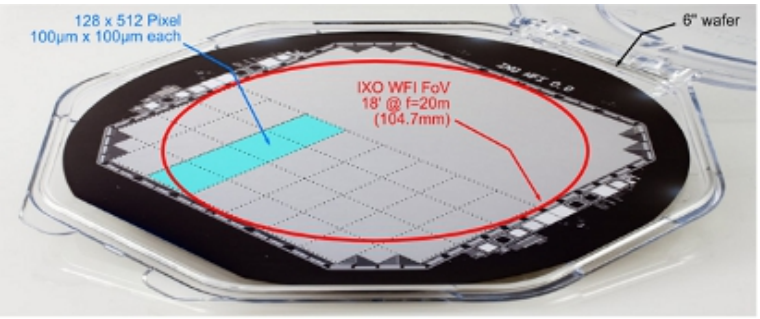

Figure 5.8: The IXO Wide Field Imager is subdivided into 16 arrays with 128 × 512 pixels, each provided with its own readout ASIC (ESA, 2010).

The Hard X-ray Imager

In order to extend the WFI energy band (0.1 - 15 keV), the HXI is mounted in a sandwich structure right behind the WFI. The WFI's quantum efficiency drops for photons of higher energy. They will pass the detector, depositing only a part or none of their energy, but photons with energies up to 100 keV will be completely absorbed in the HXI. The requirements of the HXI will be at least a 1 keV energy resolution at 40 keV and a FOV of 12′ × 12′. The detector consists of three layers. The upper two

layers consist of double sided silicon strip detectors (DSSDs), both half a milimeter thick and the lowest layer is a 0.75 mm thick double-sided strip CdTe detector. The two DSSDs act as particle background detectors and provide an overlap between the WFI and the HXI energy band. In order to shield the detector from background photons that enter the detector from the back or the sides, the HXI is surrounded from five sides by a BGO ($Bi_4Ge_3O_{12}$) anti coincidence shield. The capabilities of detecting hard X-rays is essential for studying the emission profiles of SMBH accretion discs. In the sensitivity region of the HXI the emission profiles of AGN typically show an excess, that is very likely caused by X-rays of the disc corona, reflected at the highly ionised disc. They carry information about the physical conditions in this region.

Table 5.1: The IXO instrumentation requirements for different scientific topics. The data in this table is extracted from Bookbinder (2010)

Science goal	typical flux [erg/cm^2/s]	effective area [m^2]			energy resolution		instrument
		@ 1.25 keV	@ 6 keV	@ 30 keV	eV	@ keV	
strong gravity	$5 \cdot 10^{-11}$	1.5	0.65	0.015	2.5	6	XMS (WFI/HXI)
SMBH spin	10^{-12}	1	0.65	0.015	1000	30	(WFI/HXI) (XMS)
	$5 \cdot 10^{-11}$	2.5	0.5	N/A	1200	6	XPOL
NS EOS	10^{-8}	3	0.6	N/A	150	0.3 - 6	HTRS
growth of SMBHs	$3 \cdot 10^{-17}$	3	0.65	0.015	150	1	WFI/HXI (XMS)
clusteral evolution	10^{-13}	3	0.65	0.015	2.5	6	XMS (WFI/HXI)
cosmology	$5 \cdot 10^{-4}$	1	0.1	N/A	10	6	XMS (WFI/HXI)
missing baryons	10^{-11}	N/A	N/A	N/A	0.1	0.3	XGS (XMS)

6 The Test Setup

6.1 Introduction

The test setup is a test and development environment for the IXO WFI/HXI detector. In the final configuration the central component of the test setup shall consist of a small size (64 × 64 pixel) DePFET matrix and a version of the HXI, also with reduced pixel number. As it was planned for the IXO mission, these two detectors will be mounted as a stack, the WFI in front and the HXI right behind it. This combination of a low energy and a high energy detector is an innovation in X-ray astronomy. The aim of this test setup is to put the detector through its paces in a real life detector environment and to prove whether the WFI/HXI detector is capable of meeting the required performance. According to the schedule, both detectors shall first be set up in separate test environments, the HXI in Paris at the CEA (Commissariat à l'énergie atomique) and the WFI at the Institute for Astronomy and Astrophysics in Tübingen, where also the HXI shall be implemented afterwards. In the final configuration the WFI test setup will consist of mainly three components. The detector hybrid itself, a circuit board that amplifies and digitalises the detector signal and an electronic component that commands the test setup and processes the detector data (see Figure 6.1). The hybrid in turn again consists of three components. The DePFET pixel matrix, switcher chips that switch the gate, clear gate and clear voltages on and off in the right order, and a readout chip that preamplifies the detector signal. The circuit board with the amplification stage and the analog to differential converter (ADC) is the intermediate stage concerning the signal processing. It is linked via a 16 bit wide logic bus to the event preprocessor (EPP) which was designed at the Institute for Astronomy and Astrophysics in Tübingen (IAAT) and integrated in an FPGA (see Section 6.7). Its main task is to reduce the detector data to an amount that can be processed by the telescope's telemetry system. The test setup will provide the necessary environment to test and improve the performance of the EPP. The FPGA also contains a sequencer (SEQ) and an interface controller (IFC). The SEQ synchronises and commands the whole test setup and the IFC is responsible for the communication with a computer.

A relevant part of the test setup has been developed in the context of the PhD thesis of Daniel Maier at the IAAT. The detector matrix can be operated in a vacuum chamber with a SEQ that generates the necessary clock signals. Also the programming of the switcher chips and the readout chips is done via the SEQ, as forseen for the final configuration. However, at the beginning of this works, the whole

data processing chain was missing, the communication between computer and SEQ was done via a USB link (and not as forseen via SpaceWire) and in order to prepare the test setup for the integration of the HXI, the electronics had to be removed from the back part of the vacuum chamber to the top and the sides of it. This step was already well prepared and could be carried out without major complication. In the following steps Daniel Maier concentrated on the changeover to SpaceWire communication, while the focus of this thesis was the development and integration of the circuit board with the amplification stage and the ADC. Furthermore the design of a framegenerator (see Subsection 6.7.1) for debugging purposes of the EPP was an accomplishment of this thesis. In the following sections, the single components of the setup and the developments achieved within the framework of this thesis are explained in more detail.

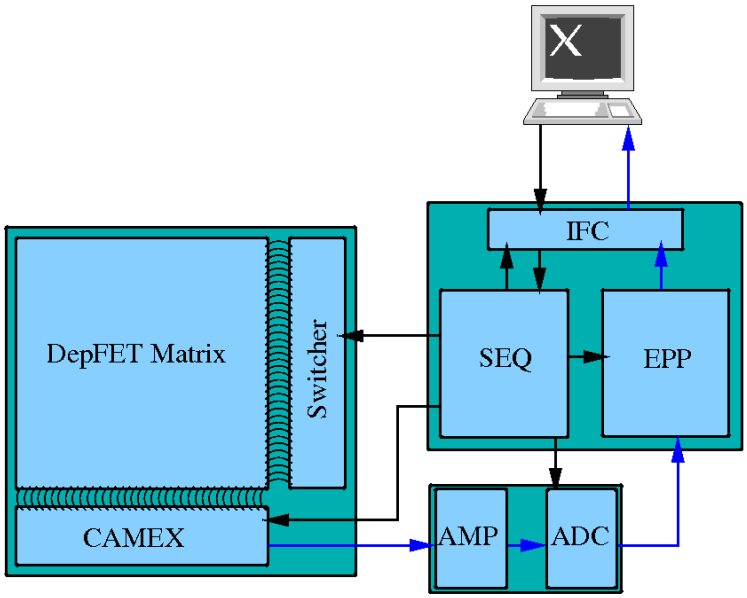

Figure 6.1: A block diagram of the IXO WFI test setup. The black arrows are marking command and clocking signals and the blue arrows the detector dataflow.

6.2 The WFI-Detector Prototype

The detector type, that was finally chosen for the IXO mission has an n-doped silicon bulk with p-doped electrodes on top and at the bottom side and another electrode at the side of the bulk. The device becomes sensitive to incident photons by sidewards depletion. The top cathode is fragmented into so called drift rings. By applying suitable voltages to the drift rings, a cone shaped potential minimum for

negative charges is formed inside the bulk, in a way that free electrons would drift inwards to the innermost part of the pixel, where they are stored in the internal gate of the also circular readout MOSFET (see also Section 4.8).

This circular MOSFET, which is illustrated in Figure 6.2 measures the internal gate charge using the source follower readout technique. In order to reset the pixel, a positive voltage pulse applied to an n-doped clear contact is used. The clear contact is sealed off from the bulk by a circular clear gate and by a p-doped implementation below the reset station.

The WFI detector at the test setup is a matrix with 500 µm x 500 µm pixel size and a thickness of 450 µm provided by the MPI Halbleiterlabor Neuperlach. It is implemented together with its front end readout and control electronic components on a ceramic hybrid. The hybrid can be cooled down by a copper cooling mask, where the hybrid is clamped in, to achieve an improved noise performance . The cooling mask is connected via copper cables to a cooling finger. The cooling finger is cooled down by $-70\,^{\circ}\mathrm{C}$ cold ethanol coming from a heat exchanger. This way, the detector can achieve a working temperature of $-45\,^{\circ}\mathrm{C}$. The detector cooling provides the problem of condensing humidity, that would effect the detector's performance and lead to short circuits. In order to avoid that, the detector is put in a chamber, where a vacuum of 10^{-6} mbar can be achieved by using a turbo molecular pump combined with a membrane backing pump. For an even better cooling, another copper mask was designed to shield the hybrid from the vacuum chambers walls, which have room temperature and emit infrared photons towards the detector.

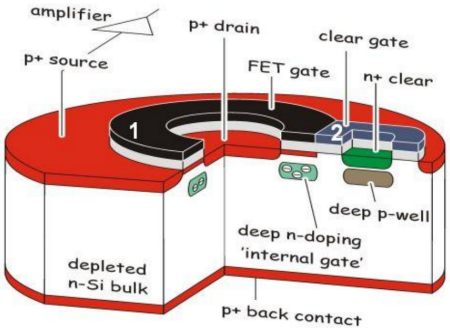

Figure 6.2: The circular structure of the WFI's readout DePFET (MPI Halbleiterlabor, Neuperlach).

6.3 Switcher

As mentioned before, to readout and reset the detector pixels, various periodically changing voltages have to be applied to the pixel's gate, clear gate and clear contact.

Therefore, two switcher chips are put on the hybrid next to the matrix. Both switcher have 2 × 64 outputs and each output can switch between two externally adjusted potentials. Figure 6.3 illustrates the functionality of the switchers.

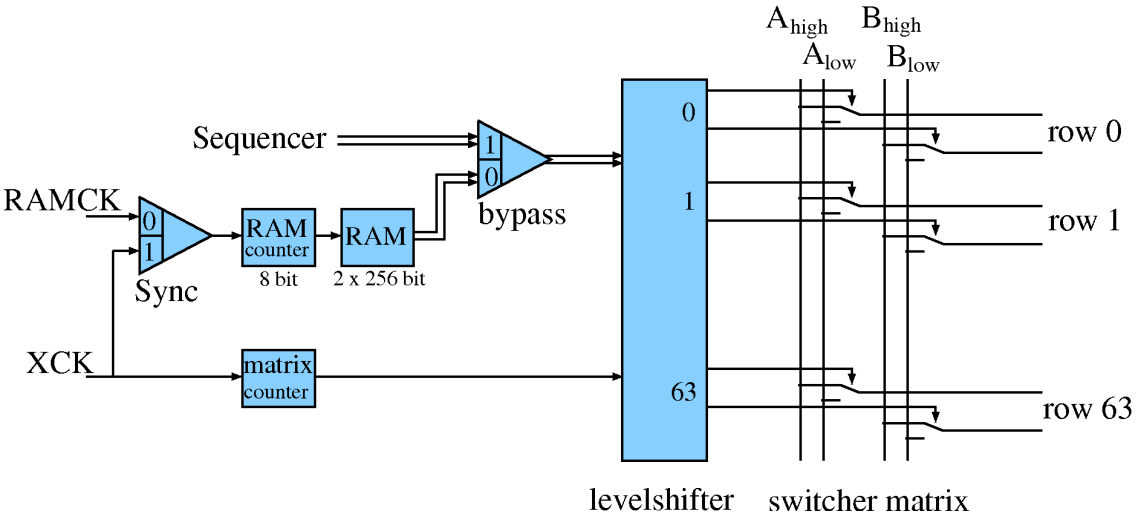

Figure 6.3: Functional diagram of a switcher. At the test setup the RAM counter and the RAM are bypassed. The switching sequence is generated by the sequencer.

When the synchronization bit (Sync bit) is set low, the RAMCK signal triggers the 8 bit RAM counter, which in turn with each RAMCK clock rising edge clocks through the 256 RAM memory units. The 2 bit wide RAM contains a programmable switching sequence. For example the value '01' would set the A output low and the B output high. The row to which this switching sequence is applied to is selected by the matrix counter. The matrix counter is clocked by the XCK signal, so the switching sequence and the row selection would have to be synchronized externally. If the Sync bit is set high, RAM counter and matrix counter will be synchronized internally by the XCK clock. In this configuration the XCK clock would not only clock the matrix counter, but would also trigger the RAM counter. To assure that both RAM and matrix counter start from zero, they can be resetted. Instead of clocking through the switching sequence saved in the RAM, the sequence can also be externally determined by the sequencer when the switchers work in bypass mode (bypass bit high). This configuration is the one that is chosen for the switcher chips of the WFI detector.

To programme the switcher chips, two eight bit shift registers are needed, a control register and a data register (see Figure 6.4).

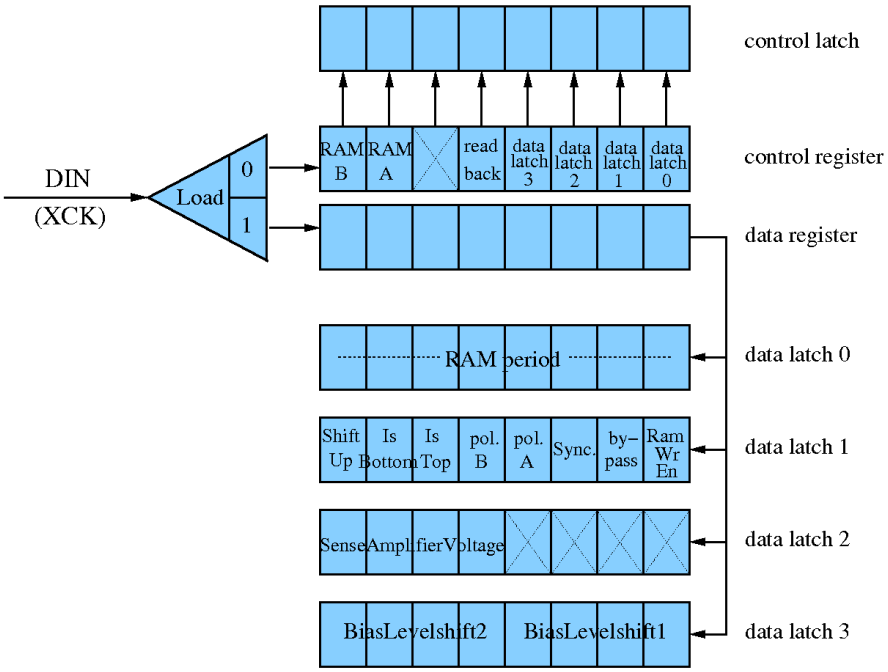

Figure 6.4: The structure of the switchers' programming unit. The XCK signal clocks the logic DIN signal through the shift registers' memory units. The state of the Load signal determines whether the control or the data register is written to.

Depending on the state of an additional Load signal, a data in (DIN) stream is either connected to the control- (Load = 0) or the data register. The data of the control register are stored in a control latch with every rising edge of the Load signal. The same happens to the binary values in the data register, but there are four data latches available to copy the data to. Apart from the Load- and the DIN signal the sequencer provides for programming a clock (CCK) and a hard reset signal. The hard reset is for erasing all data saved in the different latches and shift registers. With every rising edge of the CCK clock, the state of the DIN signal is shifted through the selected shift register. To check the configuration status of the switchers, a data output (DOUT) is either connected to the last flip flop of the control register (Load = 0) or the data register (Load = 1). It reads back the data shifted out of the registers.

The control register:

- The first 4 bits (0-3) of the control register determine in what data latch the data register value is stored.
- Bit number 4 provides the possibility to read back saved data from one of the data latches or the RAM.
- Bit 5 is not used.
- Bit 6 and 7 are for programming the RAM.

The value in data latch 0 determines the periodicity of the RAMCK counter, which can not exceed 256 times the speed of the RAMCK signal, because it is an 8 bit counter. Latch 1 is the most important one for the chosen configuration. It contains the following control bits.

data latch 1:

- For writing to the RAM, the RamWr-En, which is bit number 0 has to be set high.
- Bit 1 and 2 are the bypass and the synchronization bit (see above).
- The polarity bits 3 and 4 define the 'on' state of the switcher outputs A and B to be high or low.
- For larger detectors multiple switchers can be chained (see Figure 6.5). They can be synchronized by their so called next chip signals, which are generated when a switcher is at the end of a row selecting cycle. This signal is applied to a *start from above* or a *start from below* pin (depending on the readout direction, see bit 7) of the next chip. Bit 5 and 6 define the switcher to be the chip on top of the chain (IsTopChip) or the bottom chip (IsBottomChip).
- The last bit of latch number 1 is the ShiftUp bit. It determines whether the matrix counter should count upwards (1) or down (0).

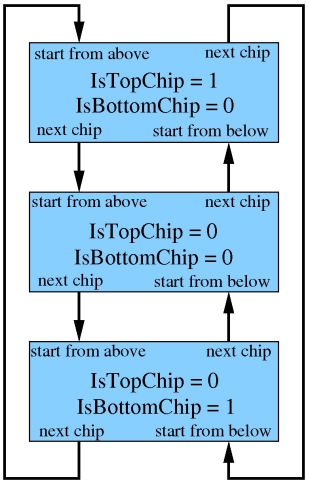

Figure 6.5: For large detectors several switchers have to be chained and synchronised. They can readout the detector in both directions, upwards (using *start from above*) and downwards (*start from below*)

12 bits of the last two data latches contain three times the binary value '1000' that are converted to analog voltages via a digital to analog converter (DAC). This voltages are the sense amplifier voltage (latch 2, bit 7-4), the BiasLevelShift1 (latch

Table 6.1: The gate, clear gate and clear voltages have to be externally adjusted

	gate	clear gate	clear
on	-2.5 V	+3.1 V	+17 V
off	+5 V	-2.7 V	-0.3 V

3, bit 3-0) and the BiasLevelShift2 (latch 3, bit 7-4) voltage. They are needed at the level shifter. To erase all data saved inside the latches and registers a hard reset has to be performed.

For operation, the switchers have to be supplied with voltages. VDDA and GNDA define the upper and lower limit for the switchable analog voltages. This range can not be more than 20 V. Because the clear pulse has to be highly positive ($\sim$ 17 V), one switcher switches the clear contacts, whereas the other one switches the gate- and clear gate voltages, which all fit quite well in a 20 V range. The digital supply voltage VDDF (+ 5 V) is the same for both switchers, as well as the digital ground GNDF.

The on and off potentials of gate, clear gate and clear contact are shown in Table 6.1.

6.4 The Readout

6.4.1 CAMEX

In the current configuration the DePFET matrix is read out by a CAMEX64 ASIC (Charge Amplifier Multiplexer), which was developed at the Halbleiterlabor (HLL) in Munich. Figure 6.6 shows its structure in a block diagram. It consists of 64 channels, one for each column for parallel processing. The stages are operated by a shift register. At the end of a readout channel the signals are serialized by a 64 : 1 multiplexer (MUX). The CAMEX works in source follower mode and its inputs are thus connected to the sources of a column (see Figure 4.15) and to a constant current source (see Figure 6.7) which is realized by a MOSFET inside the CAMEX, driven in saturation mode. The CAMEX's input stage, a charge sensitive amplifier (CSA), is capacitively coupled to the detector (C_{in}) and consists of an inverting operational amplifier with a feedback capacitor C_{f} (see Figure 6.7).

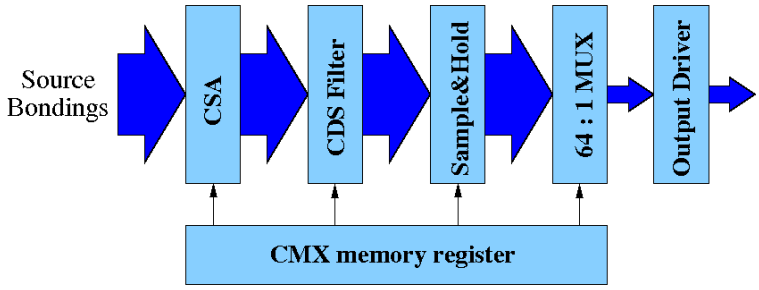

Figure 6.6: CAMEX block diagram: the different processing stages of the CAMEX readout channels are controlled by the CAMEX memory register.

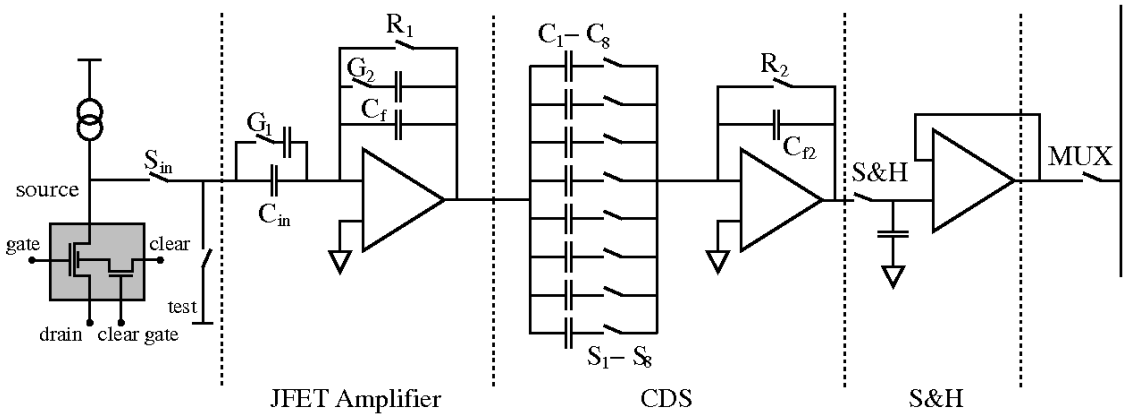

Figure 6.7: A simplified schematic of a CAMEX readout channel. In order to get different amplification gains, G_1 and G_2 can be closed and opened in four different combinations.

The amplification of the CSA stage is given by $A = C_{\text{in}}/C_{\text{f}}$, so there are four different gains possible that can be adjusted by combining the four input and feedback capacitors.

The second stage is the eightfold correlated double sampling stage. During the first step of a readout cycle the switches R_2 and Sin are closed, while $S_1 - S_8$ and R_1 are opened. The source potential of the DePFET is reflected at C_{in} and amplified. To charge the capacitors $C_1 - C_8$ with the amplifiers output voltage, switches $S_1 - S_8$ have to be closed and opened, one after another. At this time signal plus baseline charge is stored at the capacitors $C_1 - C_8$. For subtracting the baseline charge the internal gate has to be cleared (with S_{in} open) and then read out again, this time with open reset switch R_2. At the end of this cycle only the signal charge is stored in $C_1 - C_8$ and C_{f2} contains eight times the charge representing the signal. For the next readout cycle the capacitors are resetted and the signal voltage is stored at the Sample&Hold-stage before being serialized by the 64 : 1 MUX.

There are three registers to operate the CAMEX. A static one for general settings like the gain or the test mode, a shift register (128 × 16 bits) for clocking through the different processing stages and another shift register for the MUX (1 × 64 bits).

The CAMEX is already part of different astronomic X-ray missions like XMM-Newton and eROSITA, but IXO was planned to have an anti-coincidence shielding. In order to lose not too many events and to avoid pile-up a high readout speed is necessary. Currently the CAMEX at the IXO test-setup is clocked at a 38 µs line speed and even though Treis et al. (2004) reports a possible readout speed of 12 µs per line, the CAMEX is not an option for IXO where 2-4 µs (Bombelli et al., 2009) are required. Furthermore, at high readout speed multi correlated double sampling (MCDS) is inferior concerning noise compared to the switching current technique (SCT) (Porro et al., 2003). SCT is used in two other chips called ASTEROID (Active current Switching Technique Read Out In X-ray spectroscopy with DePFET), also designed for source follower readout and VELA (Very large scale integration ELectronics for Astronomy), a drain current readout chip.

6.4.2 Asteroid

The Asteroid, which was also produced at the HLL has again a charge sensitive amplifier at the front end of every readout channel, followed by an integrator and a subtraction stage (see Figure 6.8).

The schematic shows the switching sequence for a whole readout cycle. After a reset, a current proportional to the charge stored inside the internal gate of the pixel is integrated and charges the capacitors C_x and C_y while C_z is short circuited. Now, before the baseline subtraction C_x has to be resetted without discharging C_y (switch 3 open). The baseline charge is converted into a current, integrated at C_x and subtracted from C_y. At the end of this cycle there is charge stored at C_z representing only the signal.

With this double integration technique a trapezoidal weighting function is implemented, which is the optimum filter for white series noise (Gatti et al., 1990; Gatti and Manfredi, 1986). the Asteroid-chip reaches a readout time per line of ≤ 4 µs (Porro et al., 2010), which is limited by a source node settling time of about 1 µs. This settling time is needed twice, when the pixel is switched on and after the clearing.

The VELA chip dodges this settling time by using drain current readout, so no CSA is needed any more. The DePFET is read out with constant source potential and the source drain current is integrated at the integration stage. The readout cycle is the same as for the Asteroid but the drain is also connected to a current memory cell, that subtracts the offset current from the signal prior to signal processing (see Figure 6.9). For VELA a readout speed of 2 µs per line is feasible (Bombelli et al., 2009). In spite of VELA's fast processing speed the Asteroid-chip was chosen for

the IXO mission, because it can be AC-coupled to the detector device making this chip much more robust against row-to-row variations and other parameter shifts.

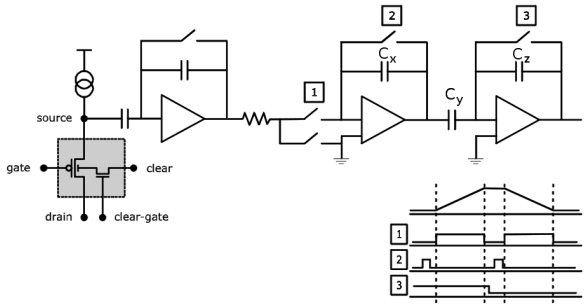

Figure 6.8: A simplified schematic of an Asteroid readout channel and its switching sequence (Lechner et al., 2010)

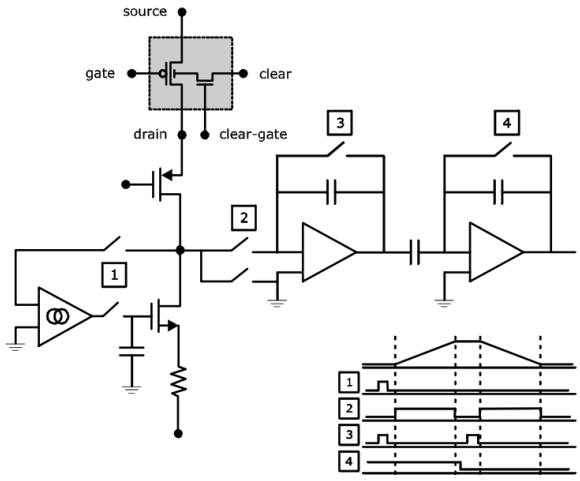

Figure 6.9: A simplified schematic of a VELA readout channel and its switching sequence (Lechner et al., 2010)

6.5 The Analog to Digital Converter

The analog to digital converter (ADC) used at the test setup for digitalising the detector signal is an AD6645 from Analog Devices. It has complementary analog input pins AIN and $\overline{\text{AIN}}$ for a differential input signal. Both analog inputs should be centred at 2.4 V and should swing around this reference in the range of ± 0.55 V.

The offset common mode of 2.4 V is generated inside the ADC and shifts both inputs to this reference at the last amplifier (AD8138) before the ADC (see Amp-stage). The signal that clocks the ADC must also be a differential one. Therefore, the single ended clock signal generated in the sequencer is transformed to a differential one at the ADC-board, and is AC-coupled into the ENCODE and $\overline{\text{ENCODE}}$ input pins. The original output signal is a 16 bit wide bus, where 14 bits represent the energy information and another one provides the information whether the pixel's energy exceeds the convertible voltage range (overrange, active high). The remaining 16^{th} bit is a data ready signal that can be used for further processing. It is set high for every converted signal. In order to decouple the digital signal from the ADC, an octal (eight in- and output pins) D-type flip-flop (74LCX574) is placed on the digital signal track. Combined with the PCB trace it typically provides a capacitive load of approximately 10 pF. The edge rising time of the digital signal is in the order of 1 ns/V, leading to 10 mA (10 pF·1 V/1 ns) dynamic currents, that flow in and out of the ADC's output pins. In order to limit the current that flows into the output stage, series resistors are placed as close as possible to the output pins. The AD6645 has separate analog (+ 5 V) and digital (+ 3 V) supply voltages, to provide the digital output from coupling into the analog signal. Also the ground is separate for the analog and digital part of the board, but joined below the ADC (see Figure 6.12), where vias connect the joined ground to a ground plane inside the 4-layer PCB and at the bottom side. This vias are also important for heat dissipation of the ADC. The ADC has a power consumption of $\sim$ 600 mA and produces considerable heat. Therefore, the ADC is thermally connected to the vias, that transport the heat to the ground plane, where it can be radiated away.

6.6 The Amplification Stage

The CAMEX output is made differential inside the readout ASIC for an improved robustness against interfering signals. The concept of differential signals is to split the primary single ended signal up into two signals, in a way that the primary signal can be reproduced by subtracting one of the differential signals from the other one. So a differential signal is actually a pair of signals, that are inversely correlated. An offset on the primary signal would lead to different DC voltages of the differential ones. If both signal lines are put close together, an interfering signal will effect both signals in the same way. So after the subtraction the interference is removed. An offset common mode voltage, which is added to both signals, doesn't change the signal information as well. The CAMEX signal has an offset common mode voltage of around 1.4 V with respect to ground and an offset of $\sim$ 200 mV, but the analog to digital converter (ADC) expects the signal to be in a certain voltage range of 2.4 V $\pm$ 0.55 V and with a certain offset. So to digitalize the signal the input stage of the ADC has not only to add an offset common mode voltage and to amplify the signal, but also to change the signal's offset.

Two solutions where suggested by our electronic group at the IAAT. The first one changed the offset of the differential signals by shifting one of them towards higher voltages, whereas from the other one it subtracted a DC voltage. This circuit was implemented on the ADC board, but turned out to be too noisy. The second solution uses only two ICs and promises a good noise performance. In order to remove the offset it converts the signal single ended, subtracts the offset by shifting the signal towards its reference potential and makes it then differential again. This circuit had to be tested, improved and implemented to the ADC board. For the first tests, a one layer board was designed and mounted on the existing ADC board, replacing the first noisy version of the amplifier stage. Figure 6.10 and 6.12 show pictures of the provisional and the final ADC board and Figure 6.11 a simplified schematic of the amplification stage. The first IC, which is the AD8130 transforms the signal to a single ended one and shifts it to an offset voltage of 2.4 V, which is the signal's reference potential at the next IC. The second component, the AD8138 makes the signal differential again and adds an offset common mode voltage V_{ref} of 2.4 V, which it gets from the ADC. This operation could actually also be done by the AD8138 with an input common mode voltage differently than the 2.4 V output common mode voltage. But this IC works best with the same input and output common mode voltage. In the AD8138 data sheet the error occuring from different input and output common modes is said to be a 1 % effect, but I have carried out tests, which show a much worse performance giving an error of the order of 10 %.

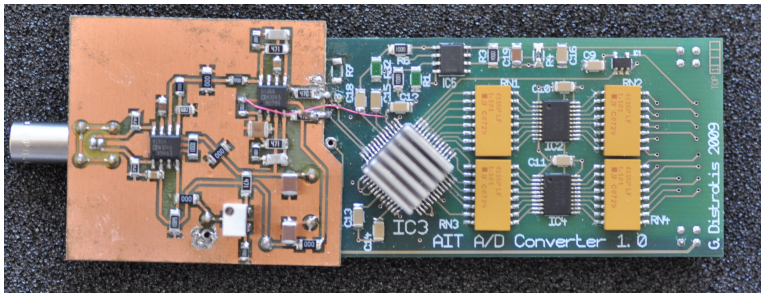

Figure 6.10: The provisional ADC-board. The amplification stage is soldered onto the copper plate, which in turn is mounted to the PCB.

6.6.1 The S2D-Converter

To test the provisional ADC board, a differential signal is necessary. Therefore, a single to differential converter board (S2D-converter) had to be designed, that transforms a single ended signal coming from a function generator to a differential one. The first version of this S2D-converter was implemented in a breadboard design. This design doesn't allow high frequency signals, because no ground planes

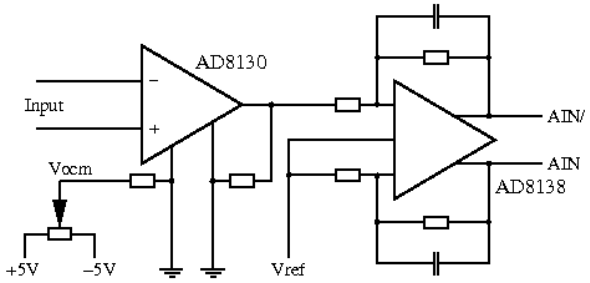

Figure 6.11: A simplified schematic of the amplification stage. Vocm can be manually adjusted, whereas Vref is generated by the ADC.

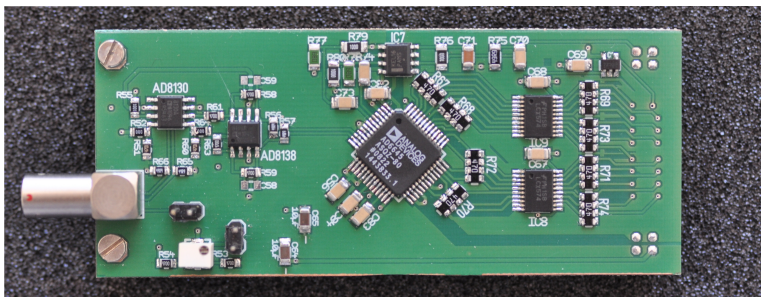

Figure 6.12: The final ADC-board. The analog part is on the left side and the digital part on the right side of the ADC

shield the signals and stray capacitances can cause the circuit to swing. Figure 6.13 shows a picture of the converter board and its schematic. The operational amplifier generates a stable voltage, which can be adapted at the adjustable resistor. It is used as offset common mode voltage for the converter boards differential output signal. For differentializing the signal, again an AD8138 is used. The inverting input can either be connected by a jumper to ground or to the adjustable offset common mode voltage, whereas the other input should be connected to a function generator. Apart from shape, amplitude and frequency, there are three settings that can be done. First, the jumper has to be set selecting either the same or different input and output common mode voltages. Second, the output common mode can be chosen and third, an offset on the differential output signal can be adjusted, by choosing different DC voltages for the two inputs.

Because of the rectangular shape of the CAMEX and Asteroid signal, all frequencies named in this thesis will correspond to rectangular signals, when not explicitely mentioned in other way. The maximum frequency, the perfboard S2D-converter can be driven at, is of the order of a few hundred kiloherz. In the current configuration,

the CAMEX puts out a signal that corresponds to a rectangular signal of 800 kHz and for testing the amplification stage at Asteroid speed, an 8 MHz signal would be necessary. Therefore, a more elaborate version of the S2D-converter was designed and implemented on a four layer printed circuit board (PCB) (see Figure 6.13). The design of this board is different with respect to the one on the breadboard. It doesn't provide the possibility of a differential signal with an offset, but the input common mode voltage can very conveniently be adjusted directly at the function generator. The output common mode can either be jumpered to be the same as the input, or manually adjusted at a voltage divider. As can be seen from the schematic, the operational amplifier THS4001 filters the DC voltage from the single ended input signal and applies it to one of the signal inputs of the AD8138, whereas the signal is also applied to the other input pin. This way the two input DC voltages are always the same and don't have to be adapted any more. This second improved version of the S2D-converter board is able to transform signals with a frequency up to 10 MHz. In Figure 6.15 the differential output signal of the converter board at Asteroid speed is shown. The periodic voltage dips at the signal have a frequency of around 100 MHz and are not introduced by the S2D-converter, but by the function generator, which provides a maximum sinusoidal frequency of 80 MHz.

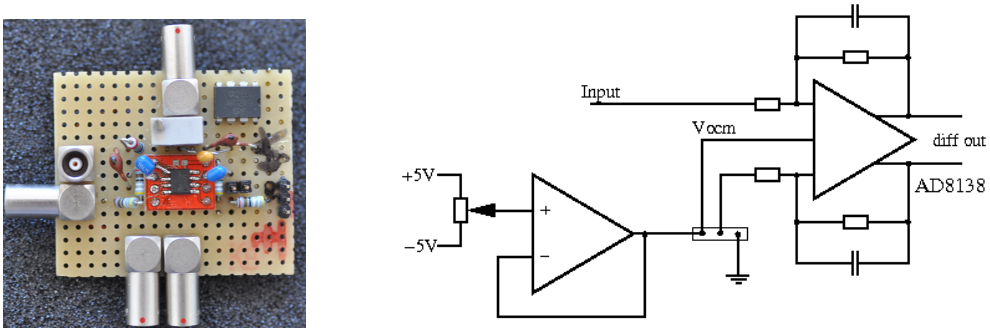

Figure 6.13: The breadboard version of the S2D-converter board. The AD8138 input which is not used by the signal can either be connected to Vocm or to ground.

6.6.2 Spice

For the development of the S2D-converter board, a simulation programme for analog electronics called Spice (Simulation Program with Integrated Circuit Emphasis) was used. Spice calculates numerical approximations to differential equations that are determined by the interconnection of electronic components. For commercial ICs most manufacturers provide spice models that can be integrated in the netlist of a circuit.

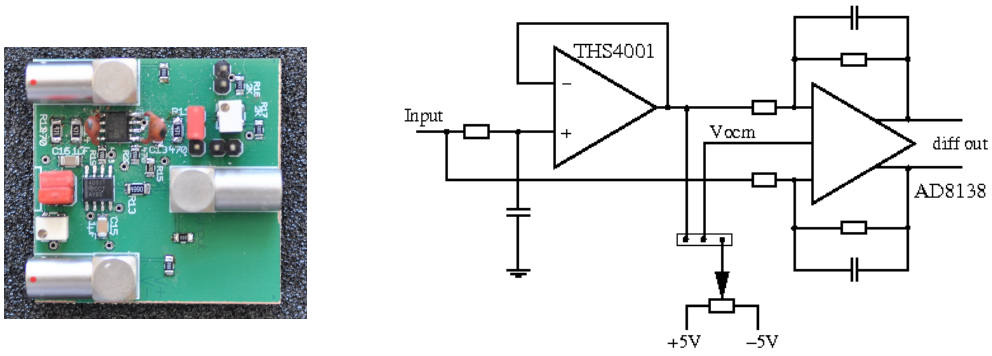

Figure 6.14: Left: The S2D-converter board. The jumper in the upper right corner can choose the offset common mode to be manually adjustable (configuration at the picture) or to be the DC-voltage of the input signal. The adjustable resistor at the left side can change the virtual ground of the input IC. Right: A simplified schematic of the S2D-converter board. The THS4001 filters the DC voltage out of the single ended signal and applies DC voltage and signal to the AD8138.

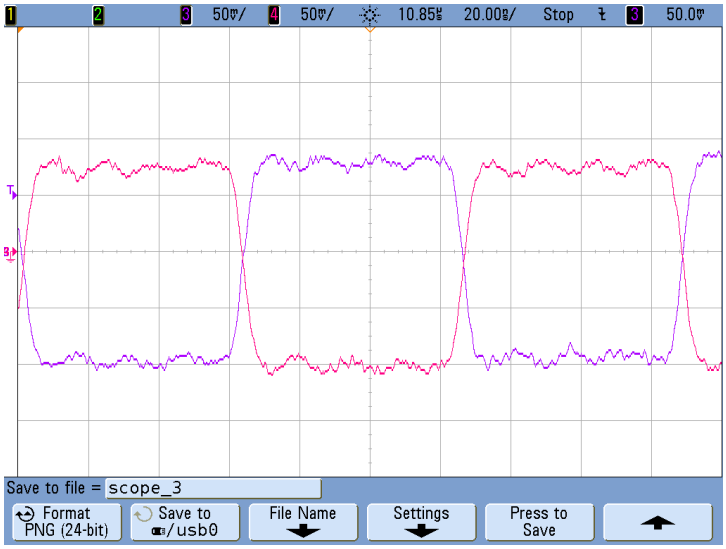

Figure 6.15: The S2D output signal. The input was a rectangular signal with 5 ns edge time, 8 MHz, 350 mV_{pp} amplitude and no offset. The offset common mode of the differential signal can be adjusted at an adjustable resistor (the one in the upper right corner in Figure 6.14). The signal is superimposed by 100 MHz dips, which are caused by the function generator's limited speed.

6.6.3 Testing the Amplification Stage

The tasks of the amplification stage are to amplify the signal, change the differential signal's offset and shift it to a common mode of $\sim 2.4\,V$ (see also Section

6.6). Furthermore, it should generate as little noise as possible, to not diminish the detectors performance. The general behaviour of the stage was tested both with a differential signal generated by the S2D-converter board and with the CAMEX signal. The removal of the offset works very well. It can be adjusted manually with mV precision and centred in the required voltage range around 2.4 V. The gain of the amplification is currently set to 1. In order to achieve the highest possible gains, the highest generated signals (corresponding to $\sim$ 15 keV photons) should be amplified in a way, that they fully exploit the voltage range that the ADC can handle. This gain should be set in the calibration phase of the test setup detector, using 15 keV photons. The noise generated by the amplification stage should not be measured using the S2D-converter board. The function generator's performance, two cables (one between function generator and S2D-converter and the other one between S2D-converter and the amplification stage) and the converter board would influence this measurement. But comparing the signal coming from the CAMEX to the signal of the amplifications stage's output (Figures 6.16 and 6.17), shows nearly no noise degradation. The periodic wiggles on the signals originate from the SCLK signal that clocks through the CAMEX memory register. The SCLK clock interferes with the signal inside the readout chip, where it is still single ended. The best way to handle this problem is probably by synchronising the SCLK clock with the clock that tells the ADC when to convert the signal applied to its input pins (PIXCLK) and to measure in between these wiggles. The switching current technique used in the Asteroid chip promises a much better noise performance compared to the CAMEX's MCDS technique (Porro et al., 2010), so this problem will probably be gone after replacing the CAMEX by the Asteroid.

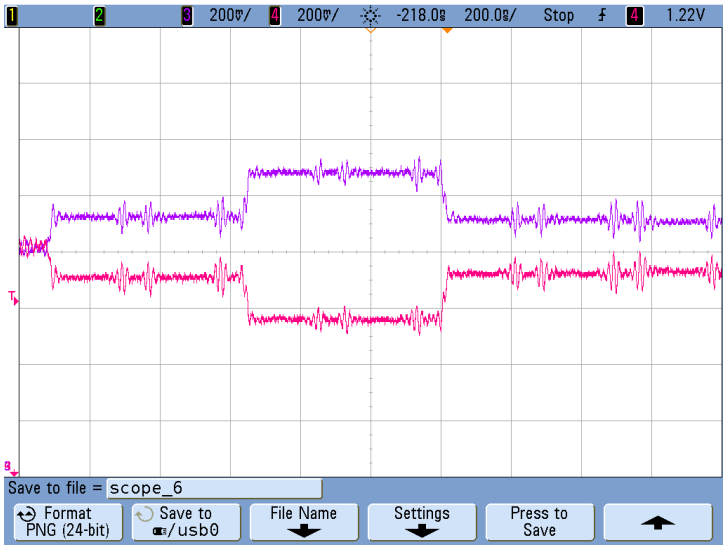

Figure 6.16: The differential CAMEX signal. The signal has an offset common mode of $\sim 1.4\,\mathrm{V}$ and is superimposed by switching noise. The CAMEX signal offset is $\sim 200\,\mathrm{mV}$.

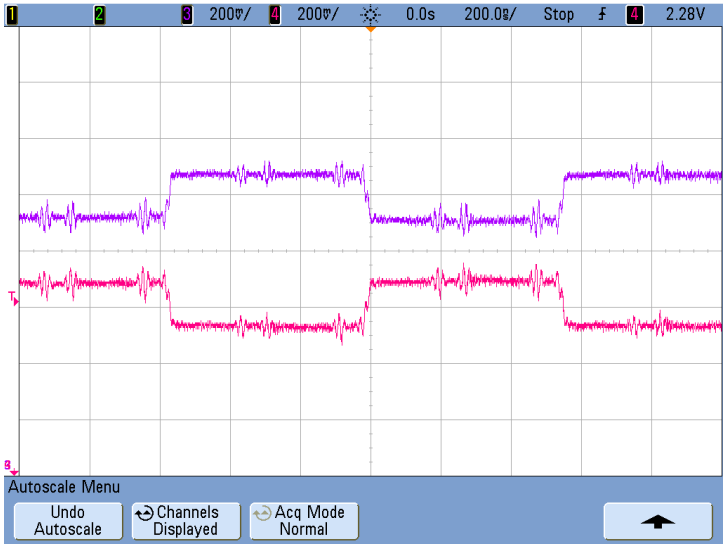

Figure 6.17: After the CAMEX signal has passed the amplification stage, there is nearly no degradation concerning noise. The offset of the differential signal can easily be adjusted at an adjustable resistor at the ADC-bord. The signal has an offset common mode of $\sim 2.46\,\mathrm{V}$, given by the ADC.

6.7 The Event Preprocessor

The electronics around the WFI has to solve one major task, which is to process high data rates, resulting from an imaging detector with a large number of pixels combined with high time and energy resolution. The bottleneck of the processing electronics is the telemetry system, that sends the data from space to Earth. The maximum transfer speed of $\sim 8\,\mathrm{Mbits/sec}$ (Barcons et al., 2011) is much too low for the whole data stream. The Asteroid is able to readout a whole detector frame of the test setup DePFET array with 64×64 pixels 4000 times a second. The energy information of each pixel is encoded with 14 bits by the ADC. So even without time stamp and pixel number the small sized test setup matrix would produce

$$64 \times 64 \times 4000/\mathrm{s} \times 14\,\mathrm{bits} \approx 750\,\mathrm{Mbits/s}$$

To realize the whole potential of the detector, the data rate has to be reduced on board of the satellite, which is done by the event preprocessor (EPP).

The EPP is based on semiconductor technology and is programmed in a hardware component called field programmable gate array (FPGA). FPGAs are integrated circuit (IC) components made out of a large number of logic cells, each consisting of a programmable look up table (LUT) (for which four is the most commonly used number of inputs), a D-type flip-flop and a $2:1$ multiplexer. The LUT's output, which is set high or low, depending on whether the input value matches the truth table saved inside the LUT, is applied to the multiplexer and can be saved in the flip-flop (see Figure 6.18). By combining and programming these logic cells, the FPGA can take the roll from simple logic gates up to complex structures like microprocessors. And that makes the development phase much easier compared to the development of a specific IC.

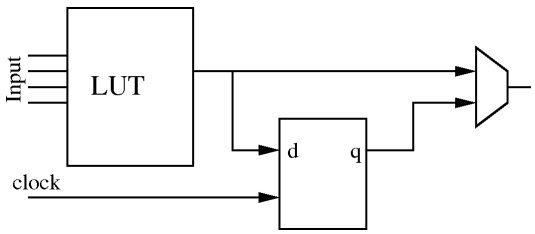

Figure 6.18: The logic cell of an FPGA consists of a lookup table, a D-flip-flop and a $2:1$ multiplexer.

When used in space, the great benefit of FPGAs compared to a CPU (central processing unit) is its radiation hardness. The small structures of a CPU are susceptible to radiation damages, whereas FPGAs are nowadays also produced as radiation

hard ICs. Additionally the aforementioned ability of parallel processing and the low power consumption compared to CPUs are good arguments for an FPGA based EPP.

For processing, the event data has to go through five stages as shown in the block diagram in Figure 6.20. The five processing stages do energy corrections and set flags on an additional flag bus when certain conditions are fulfilled. At the end of the processing pipeline the rrogrammable pixel filter unit (PPFU) rejects those events with flags that indicate them to be invalid events.

The Pixel Address Generator Unit

Inside the pipeline the events position correspond to their position on the detector. But before being sent to Earth the data has to pass a programmable flag filter mask, that rejects most of the events. So to not lose the events position information, the pixel address generator unit (PAGU) provides the events with their pixel number.

The Pixel Correction Unit

The second stage is the pixel correction unit (PCU), that performs an offset correction. In spite of the correlated double sampling technique of the readout ASIC (see also CAMEX and Asteroid), all pixels show an individual baseline level, caused by leakage currents and variations in geometry and doping of the different pixels. This offset value has to be subtracted from the signal value. To determine the offset for each pixel, a calibration measurement with an unexposed detector is done in the following way. In order to eliminate row to row variations of the signal, a common mode correction is performed first (see common mode correction unit). After the removal of the common mode, the pixel data of the unexposed detector correspond to their offsets. By repeating this measurement, the influence of statistic fluctuations can be diminished. The offset values are saved in an offset map inside the EPP and can then easily be subtracted from the signal data. The offset map contains 16 bit information for each pixel. The offset energy value is encoded with the 14 least significant bits, and the most significant bit indicates whether it is a bad pixel (high) or not (low). The remaining bit is not used. Bad pixels are pixels that are insensitive, or pixels that are always flooded with charges independent on whether the pixel got hit by a photon. For bad pixels the PCU sets a bad pixel flag to the event on a two bit wide flag bus. The second flag of the bus is for MISFIT and MIP events. MISFIT events are events that happen during readout and are therefore represented by a signal of reversed sign, whereas minimal ionizing particles (MIPs) are charged particles that deposit their energy along their path through the detector. They can be spotted by comparing the pixel energy to a suitably selected energy threshold. The MIP&MISFIT flag is set high for events that exceed this threshold.

The Common Mode Correction Unit

Since the detector is readout row wise, variations in supply voltages of the readout chip would effect the gain of all pixels of one row in the same way. A first order correction of this so called common mode effect can be done after the events passed the PCU in the common mode correction unit (CMCU). In order to do this correction, all pixel data of one row is sorted by its energy value. The energy value of the pixel, which is in the middle after the sorting is then subtracted from all other energy values, assuming that in one frame time only few pixels of a row get hit by photons. This energy value is called median. For an even number of pixels, of course, there is never a pixel in the middle. Therefore, the median is then chosen to be the arithmetic average of the two innermost pixel energy values after the sorting. In general sorting algorithms are lengthy processes. But in this case the sorting time can be shortened by taking advantage of the FPGAs ability to process in parallel (Christmann, 2011).

The Energy Threshold Analysing Unit

Because of the short signal integration time, very few pixels will be exposed per frame. Therefore, the energy threshold analysing unit (ETAU) promises a very efficient data reduction. The ETAU checks if the energy value exceeds a low energy threshold. If this threshold is adapted appropriately, all unexposed pixel energy values can be marked with a low energy threshold flag. Excluded from this check are all those pixels, which are next to a pixel exceeding this threshold (except MIP events). If an event occurs close to a pixel boundary a small fraction of a signal charge could be stored in such a neighbouring pixel. In order to get the complete photon energy, neighbour pixels are checked for another, the so called neighbour energy threshold, which should be chosen to be even lower than the low energy threshold. To mark this neighbour events, another flag can be set high or low depending on whether the energy value falls below or exceeds the neighbour energy threshold. So after passing the ETAU the number of flags is expanded from two to four.

The Pattern and Trace Analyzer Unit

When two photons hit the detector during one frame close to each other, in a way that they can't be distinguished by their location any more (pile up), the deposited energy would be falsely interpreted as the energy of just one photon. To avoid that short integration times are useful. However, if pile up occurs anyway, the Pattern and Trace Analyzer Unit (PTAU) can spot these multiple events. The detector pixel size is designed for small oversampling to ensure, that the angular resolution is limited by the optics rather than by the detector (see Lechner et al. (2010)). Single photon events can only occur with five different patterns, which are shown

in Figure 6.19.

All events that correspond to different patterns receive an invalid flag. Of course, two photons could also hit the detector producing a valid pattern and without exceeding the high MIP threshold. But this contribution to the pile up becomes more and more unlikely with higher readout speed. For very bright astronomical sources, the detector can also be set in window mode, where only a selected area of the detector matrix is readout, making shorter exposure times feasible. Apart from pattern filtering, the PTAU also generates a 32 bit time stamp, which is the same for all pixels of one row and it sorts out all pixels marked as invalid events by their flags.

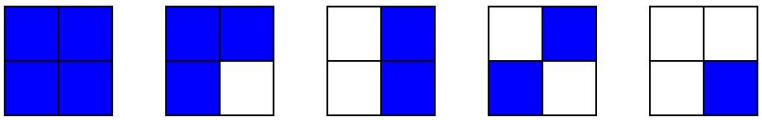

Figure 6.19: The five valid patterns including their rotations. All differing patterns are rejected in the PTAU.

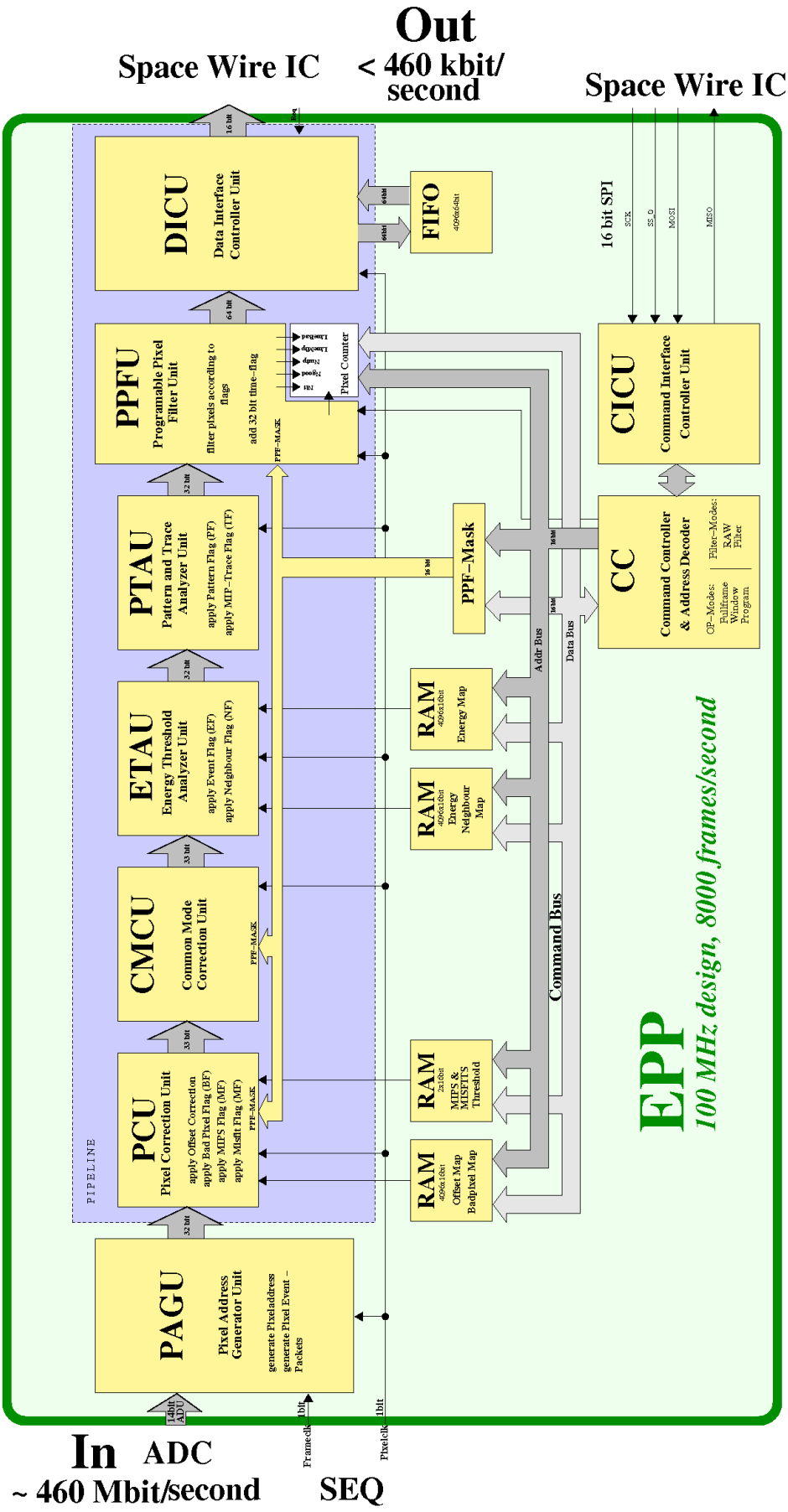

Figure 6.20: The processing pipeline of the EPP has to reduce the data by at least a factor of 1000 (Thomas Schanz).

Table 6.2: A bug, probably located in the IFC, causes an interchanging of pixel numbers. Actually each event should account for an energy value corresponding to the pixel number.

pixel number	energy value
0	0x1
1	0x0
2	0x3
3	0x2
.	.
.	.
.	.
62	0x3F
63	0x3E

6.7.1 The Framegenerator

Even though the performance of an FPGA design can be simulated, errors can occur easily in such a complex system. The problem with testing the EPP directly with detector data is the fact, that the incoming data is not known. So to assure that the EPP processes the data the way it should, the data at the EPP's input and output have to be compared. Therefore, another FPGA design was implemented in a Spartan 3 FPGA, that simulates the ADC producing data that can be processed by the EPP. This FPGA which from now on will be referred to as framegenerator is put piggyback on top of an adapter board, so it can replace the ADC-board. The framegenerator's design mainly consists of a $16 \times (64^2 \times 6)$ bit ROM, that is externally clocked by the sequencer and is connected to the EPP by a 16 bit wide data bus, representing the 14 bit energy information plus 2 bits used as next pixel (data ready) and over range signal (see also ADC). The depth of the ROM contains six data frames. The frame generator is a valuable debugging tool. All processing stages can be tested by saving suitable frames in the framegenerator's ROM. One bug that had been found this way is the interchanging of pixel addresses that probably occurs in the interface controller (see Section 6.8). For the test that led to the discovery of this bug, the framegenerator's ROM contained data that corresponded to hexadecimal energy values of '0' for pixel number 0, '1' for pixel number 1 ... and so on. At the output of the IFC with the EPP in bypass mode the pixel values were interchanged as Table 6.2 indicates.

Tests of the different processing stages of the EPP were also performed, but since they were influenced by the bug described above, it was not in all cases to see whether they yielded the expected result. These tests will be performed again after the removal of the bug. What exactly causes this error is still uncertain. But since this error is reproducible, simulating the EPP VHDL code with a tool like Modelsim and looking for this specific bug will probably lead to quick success.

6.8 The Interface Controller

In the recent design, the interface controller (IFC) is implemented in the same FPGA as the EPP and the SEQ. It links the WFI detector assembly via a SpaceWire core to the rest of the spacecraft. All communication and data transfer will be done across this component. Simplified can be said, that the IFC contains six subcomponents (see Block Diagram 6.21). The aforementioned SpaceWire core, a receiver, a sender and three control components for the EPP, the SEQ and the housekeeping ADC. The latter is the control component for housekeeping data, which will be digitalized by an ADC additional to the one for the detector data. Housekeeping data could for example be the temperature of the detector matrix, but since at the moment the housekeeping component is not part of the test setup, it will not be part of this thesis. The SpaceWire core is in charge of the SpaceWire communication in both directions. At the test setup it sends data packages coming from the sender via SpaceWire to a computer, but it also hands control data to the receiver, which in turn distributes the packages to the different control components. For further information about the SpaceWire protocol and data encoding, reference is made to an ESA information site about SpaceWire communication (http://spacewire.esa.int). The EPP-control collects science data from the EPP and passes it to the sender. Controlling the EPP is not done by the EPP-control, but by the SEQ (see also Section 6.9). The control component of the SEQ is the SEQ-control. It is connected to the SEQ by an SPI interface. To distribute the data correctly the receiver needs to get addresses for the different control components (see Table 6.3). Data sent to the echo address, are directly sent back via the sender. As mentioned before, the EPP is controlled via the SEQ. Therefore, the EPP-control doesn't receive data, this address is always a sender (Gebhardt, 2009).

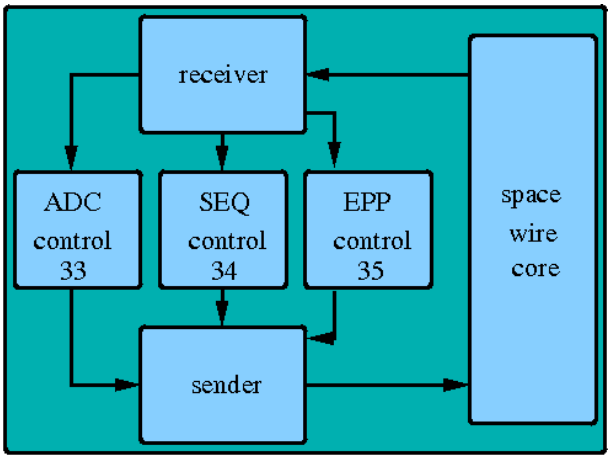

Figure 6.21: The IFC: the SpaceWire core inside the IFC enables the SpaceWire communication with the test setup. The receiver distributes the incomming data to the different control components and the sender collects data comming from the detector side and hands them to the SpaceWire core.

Table 6.3: The IFC addresses for the different control components.

address	component
33	ADC control
34	SEQ control
35	Science data
30	echo

6.9 The Sequencer

The sequencer (SEQ) is the central component of the test setup. It programmes the readout chip and the switchers, commands the EPP and synchronizes the whole detector assembly by providing all components with clock signals (see Figure 6.1). In order to command and programme the various registers and write on the EPP RAMs, containing offset map, the energy map and the neighbour energy map, there are different track switches inside the SEQ, which have to be set. Table 6.4 shows the address values for the registers and memories, as well as the different commands. For programming the CAMEX memory and status register, values have to be sent to the corresponding address and then to be uploaded to the CAMEX by the SEQ command *CAMEX upload*. For the switchers it is the same, just the matrix counter (*SW reset*) and the latches registers (*SW hard reset*) have to be resetted first.

Table 6.4: Programming commands for the sequencer.

register	**address**	**(default) value (hex)**	**meaning**
SEQ command register	33F2	FF00	reset
		FF80	programme mode
		FFF0	standby
		FFFF	work
		FF1F	CMX upload
		FF3F	sw upload
		FFF3	sw reset
		FFF4	sw hard-reset
		FF01	full frame
		FF05	window mode
SW status reg 0	33E8	not used	
SW status reg 1	33EA	4951	
SW status reg 2	33EC	5458	
SW status reg 3	33EE	4414	
CMX memory register	3400	A000	
	...	...	
	347F	A000	
CMX status register	34F4	000A	
EPP command register	3100	FF00	reset
		FF80	programme mode
		FFF0	standby
		FFFF	work
		FFFC	diagnose mode
EPP status register	3004	0000	full frame
		0001	window mode
EPP offset register	0000	0004	
	...	...	
	0FFF	0004	
EPP neighbour map	1000	03E8	
	...	...	
	1FFF	03E8	
EPP energy map	2000	04B0	
	...	...	
	2FFF	04B0	
EPP MIPs register	3000	36B0	
EPP Misfit register	3001	0080	
EPP PPF mask	3002	FFFF	

6.10 IDEF-X

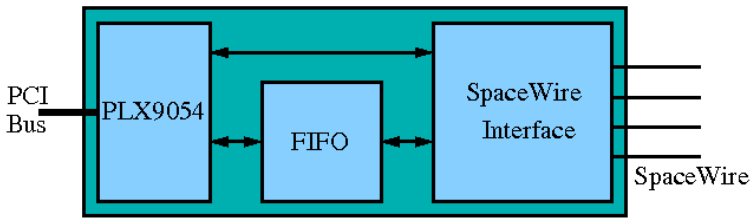

Figure 6.22: The IDEF-X hardware is the interface between computer and SpaceWire link.

On the computer side of the test setup the communication is done with IDEF-X, which is a software that transmits and receives signals via a SpaceWire connection to the detector. The hardware component between computer and the SpaceWire link is a PCI-card (Peripheral Component Interconnect) consisting of a PLX9054, which is a 32 bit PCI bus master interface chip, a Fifo (First-in-first-out) memory, serving as a temporary buffer and a SpaceWire interface (see Figure 6.22). In order to command the detector setup, the IDEF-x commands have to be written in so called batch files with '.txt' endings. On the whole, there are two types of commands. Some to control the PCI-card and some to command the detector. The commands for the PCI-card begin with an 'S', followed by a number between '00' and '06'. Their meanings are:

S00: label X

S01: wait for X ms

S02: X-fold loop at label X

S03: loop at label X

S04: stopping point

S05: start acquisition

S06: stop acquisition

For example 'S01 10' would mean: 'wait for 10 ms'. The most important commands for the test setup requirements are 'S05' and 'S06'. The commands to be transmitted to the detector are framed inside the batch file by an 'I' for 'initial' and an 'E' for 'ending'. In between them is the actual code, consisting of a four block package structure, divided by an 'end of package' command sequence ('0100'). In the first block every package contains the address of the control component (see table 6.3), so the IFC knows how to distribute the data. The second block contains

the information about the register the data should be written to or read from. This addresses are summarised in table 6.4. The third block defines whether the data should be read from ('C003') or written to ('4182') the chosen address and the last block contains the data itself. In the case of a read command this last block has to contain some dummy data in order to keep the four block structure.

A typical batch file is for example the write-CAMEX-register file:

S 05

I

& start programme mode
& IFC address
# 0034

& register address
# 0033
# 00F2

& write mode
# 0041
# 0082

& value # 00FF
# 0080

& end of package
# 0100

& write CAMEX register
& IFC address
# 0034

& register address
# 0034
# 0000

& write mode
# 0041
# 0082

& value
# 00A0
# 0000

0100

& go into standby mode
# 0034

0033
00F2

0041
0082

00FF
00F0

0100

E

S 06

7 Summary and Outlook

The goal of this thesis was to expand the IXO WFI test setup and prepare it for the integration of the HXI. The HXI will be mounted behind the WFI. Therefore, the removal of the electronics from the back of the vacuum chamber to the top and the sides of it was a necessary step in order to allow the integration of the HXI. The integration of the amplification stage and the ADC into the processing chain was a major step forward to complete the detector assembly. The general behaviour of the amplification stage was successfully tested. It is able to amplify the signal, remove its offset and to shift it into the required voltage range. Furthermore it provides an excellent noise performance. The development of the S2D-converter board was necessary to provide the amplification stage with differential signals. It is a valuable tool that allows to test the amplification stage with rectangular signals up to 10 MHz. Also the EPP and the IFC have been integrated in the test setup, so the integration of hardware components, necessary to drive the detector, is complete and the test setup is fully operational. The framegenerator provides the possibility to test the EPP with a fixed set of input data that can be adapted, depending on the kind of test that shall be performed. The benefit of this component is the exact knowledge of the data applied to the EPP's inputs, so comparing the EPP's input and output yields the knowledge whether it processes the data the way it should. The framegenerator is therefore a valuable tool for debugging purposes.

However, there is still a lot of work to do. The switching noise of the CAMEX chip is a problem that can be solved by synchronising the analog to digital conversion with the SCLK signal, which causes the noise. Since the CAMEX will be replaced by the Asteroid chip, however it's probably just a temporary problem. The amplification stage is designed in a way, that it can be used also for the Asteroid chip, with just a few small and simple changes. The amplification of the detector has to be adapted to the detector's energy range. That can easily be done by replacing two resistors at the ADC-board. Even the small size test setup detector matrix with the "slow" CAMEX chip produces an amount of data, that can not be sent via the SpaceWire link in real time, when the amount of data is not reduced. In order to achieve sufficient data reduction with the EPP, the energy thresholds and the default values in the different maps of the EPP have to be adapted to the signals of the matrix. For full completeness of the test setup, there are two more steps to go. The changeover to the Asteroid readout chip is necessary to achieve the readout speed required for the scientific goals of the IXO mission and the integration and synchronisation of the HXI, in order to expand the detector's energy band. The IXO test setup will for the first time provide the possibility to test such a sandwich structure detector.

List of Figures

3.1 Bremsstahlung Spectrum . . . 7
3.2 Characteristic X-ray Emission . . . 7
3.3 X-ray-Matter Interaction . . . 10
3.4 Compton Effect . . . 11
3.5 Atmospheric Absorption . . . 12
3.6 Wolter optic . . . 13
3.7 Total Eclipse of the Sun . . . 15
3.8 Coronal Loops . . . 16
3.9 SNR N49 . . . 17
3.10 Pulsar . . . 17
3.11 Cassiopeia-A . . . 24

4.1 Band Structure . . . 27
4.2 Doping of Semiconductors . . . 27
4.3 Non Biased pn-Junction . . . 28
4.4 Forward Biased pn-Junction . . . 28
4.5 Rewerse Biased pn-Junction . . . 29
4.6 Sidewards Depletion . . . 30
4.7 Potential (Sidewards Depletion) . . . 31
4.8 pn-CCD . . . 32
4.9 MOS-Strucure . . . 33
4.10 JFET . . . 34
4.11 JFET Current-Voltage Characteristic . . . 34
4.12 MOSFET . . . 35
4.13 MOSFET Current-Voltage Characteristic . . . 36
4.14 DEPFET . . . 37
4.15 DePFET Matrix in Source Follower Readout . . . 38

5.1 IXO Effective Area . . . 42
5.2 IXO FMA . . . 43
5.3 SGO . . . 44
5.4 IXO XGS . . . 45
5.5 SDD Macro Pixel . . . 46
5.6 HTRS . . . 46
5.7 XMS Sensor . . . 47
5.8 IXO WFI . . . 48

6.1 Test Setup Block Diagram . . . 52
6.2 Readout of a DePFET Pixel . . . 53
6.3 Switcher Function Diagram . . . 54
6.4 Programming Unit of a Switcher . . . 55
6.5 Chained Switchers . . . 56
6.6 CAMEX Block Diagram . . . 58
6.7 CAMEX Schematic . . . 58
6.8 Schematic of the Asteroid . . . 60
6.9 Schematic of VELA . . . 60
6.10 Provisional ADC-board . . . 62
6.11 Schematic of the Amplification Stage . . . 63
6.12 The ADC-board . . . 63
6.13 Provisional S2D-Converter Board . . . 64
6.14 S2D-Converter Board . . . 65
6.15 S2D Output Signal . . . 65
6.16 The CAMEX Signal . . . 67
6.17 The CAMEX Signal after the Amplification Stage . . . 67
6.18 FPGA Logic Cell . . . 68
6.19 Patterns . . . 71
6.20 EPP Block Diagram . . . 72
6.21 IFC Block Diagram . . . 75
6.22 PCI-card . . . 77

List of Tables

5.1 IXO Requirements 50

6.1 Gate, Clera Gate and Clear Voltages 57
6.2 The IFC bug 73
6.3 IFC Addresses 75
6.4 SEQ Commands 76

Bibliography

S. W. Allen, R. W. Schmidt, H. Ebeling, A. C. Fabian, and L. van Speybroeck. Constraints on dark energy from Chandra observations of the largest relaxed galaxy clusters. *Monthly Notices of the Royal Astronomical Society*, 353:457–467, September 2004.

S. W. Allen, D. A. Rapetti, R. W. Schmidt, H. Ebeling, R. G. Morris, and A. C. Fabian. Improved constraints on dark energy from Chandra X-ray observations of the largest relaxed galaxy clusters. *Monthly Notices of the Royal Astronomical Society*, 383:879–896, January 2008.

X. Barcons, D. Barret, M. Bautz, J. Bookbinder, J. Bregman, T. Dotani, K. Flanagan, R Fraga-Encinas, J. Grady, H. Kunieda, D. H. Lumb, K. Mitsuda, K. Nandra, T. Ohashi, L. Piro, N. Rando, L. Strüder, T. Takahashi, T. G. Tsuru, and N. E. White. International X-ray Observatory (IXO) Assessment Study Report for the ESA Cosmic Vision 2015-2025. *ArXiv e-prints*, February 2011.

E. Berti and M. Volonteri. Cosmological Black Hole Spin Evolution by Mergers and Accretion. *The Astrophysical Journal*, 684:822–828, September 2008.

J.D.E. Beynon and D.R. Lamb. *Charge-coupled devices and their applications*. McGraw-Hill, 1980.

L. Bombelli, C. Fiorini, and M. Porro. Fast DEPFET current readout for X-ray astronomy missions. *Nuclear Instruments and Methods in Physics Research A*, 604:679–683, June 2009.

L. Bombelli, C. Fiorini, M. Porro, J. Treis, and T. Lauf. VELA: A fast DEPFET readout circuit for the IXO mission. *Nuclear Instruments and Methods in Physics Research A*, 617:316–318, May 2010.

J. Bookbinder. The International X-ray Observatory - RFI#2. *ArXiv e-prints*, March 2010.

S. Chandrasekhar. The Maximum Mass of Ideal White Dwarfs. *The Astrophysical Journal*, 74:81–+, July 1931. doi: 10.1086/143324.

Stefan Christmann. Design and implementation of an fpga-driven, hardware-based realtime data reduction system for pixelated photon detectors. *diploma thesis*, 2011.

C. W. Danforth and J. M. Shull. The Low-z Intergalactic Medium. III. H I and Metal Absorbers at z ¡ 0.4. *The Astrophysical Journal*, 679:194–219, May 2008.

J. W. den Herder, A. C. Brinkman, S. M. Kahn, G. Branduardi-Raymont, K. Thomsen, H. Aarts, M. Audard, J. V. Bixler, A. J. den Boggende, J. Cottam, T. Decker, L. Dubbeldam, C. Erd, H. Goulooze, M. Güdel, P. Guttridge, C. J. Hailey, K. A. Janabi, J. S. Kaastra, P. A. J. de Korte, B. J. van Leeuwen, C. Mauche, A. J. McCalden, R. Mewe, A. Naber, F. B. Paerels, J. R. Peterson, A. P. Rasmussen, K. Rees, I. Sakelliou, M. Sako, J. Spodek, M. Stern, T. Tamura, J. Tandy, C. P. de Vries, S. Welch, and A. Zehnder. The Reflection Grating Spectrometer on board XMM-Newton. *Astronomy and Astropysics*, 365:L7–L17, January 2001.

R.D. Evans. *The atomic nucleus*. International series in pure and applied physics. McGraw-Hill, 1955.

U. Fano. Ionization yield of radiations. ii. the fluctuations of the number of ions. *Physical Review*, 72:26–29, July 1947.

E. D. Feigelson, E. J. Schreier, J. P. Delvaille, R. Giacconi, J. E. Grindlay, and A. P. Lightman. The X-ray structure of Centaurus A. *The Astrophysical Journal*, 251: 31–51, December 1981.

P. Fischer, W. Neeser, M. Trimpl, J. Ulrici, and N. Wermes. Readout concepts for DEPFET pixel arrays. *Nuclear Instruments and Methods in Physics Research A*, 512:318–325, October 2003.

W. Forman, C. Jones, L. Cominsky, P. Julien, S. Murray, G. Peters, H. Tananbaum, and R. Giacconi. The fourth Uhuru catalog of X-ray sources. *The Astrophysical Journal*, 38:357–412, December 1978.

W. Forman, J. Schwarz, C. Jones, W. Liller, and A. C. Fabian. X-ray observations of galaxies in the Virgo cluster. *The Astrophysical Journal*, 234:L27–L31, November 1979.

Kai Freund. Characterisation of specific parameters of the framestore pn-ccd for erosita. *diploma thesis*, 2008.

E. Gatti and P. F. Manfredi. Processing the signals from solid-state detectors in elementary-particle physics. *Nuovo Cimento Rivista Serie*, 9:1–146, January 1986.

E. Gatti and P. Rehak. Semiconductor drift chamber. *Nuclear Instruments and Methods in Physics Research*, 225:608–614, September 1984.

E. Gatti, M. Sampietro, and P. F. Manfredi. Optimum filters for detector charge measurements in presence of 1/f noise. *Nuclear Instruments and Methods in Physics Research A*, 287:513–520, February 1990.

Henry Gebhardt. Development of data acquisition and detector controller electronics for the low energy x-ray detector of the simbol-x space mission. *diploma thesis*, 2009.

R. Giacconi, H. Gursky, F. R. Paolini, and B. B. Rossi. Evidence for x Rays From Sources Outside the Solar System. *Physical Review Letters*, 9:439–443, December 1962.

R. Giacconi, H. Gursky, and L. P. van Speybroeck. Observational techniques in x-ray astronomy. *American Science and Engeneering*, 6:373–+, 1968.

R. Giacconi, W. P. Reidy, G. S. Vaiana, L. P. van Speybroeck, and T. F. Zehnpfennig. Grazing-Incidence Telescopes for X-Ray Astronomy. *American Science and Engineering*, 9:3–57, February 1969.

R. Giacconi, E. Kellogg, P. Gorenstein, H. Gursky, and H. Tananbaum. An X-Ray Scan of the Galactic Plane from UHURU. *The Astrophysical Journal*, 165:L27+, April 1971.

R. Giacconi, G. Branduardi, U. Briel, A. Epstein, D. Fabricant, E. Feigelson, W. Forman, P. Gorenstein, J. Grindlay, H. Gursky, F. R. Harnden, J. P. Henry, C. Jones, E. Kellogg, D. Koch, S. Murray, E. Schreier, F. Seward, H. Tananbaum, K. Topka, L. Van Speybroeck, S. S. Holt, R. H. Becker, E. A. Boldt, P. J. Serlemitsos, G. Clark, C. Canizares, T. Markert, R. Novick, D. Helfand, and K. Long. The Einstein /HEAO 2/ X-ray Observatory. *The Astrophysical Journal*, 230:540–550, June 1979.

T. Güver, F. Özel, A. Cabrera-Lavers, and P. Wroblewski. The Distance, Mass, and Radius of the Neutron Star in 4U 1608-52. *The Astrophysical Journal*, 712: 964–973, April 2010.

A. Hanslmeier. *Einf Hrung in Astronomie Und Astrophysik*. Spektrum Akademischer Verlag, 2011.

C. Jones, E. Mandel, J. Schwarz, W. Forman, S. S. Murray, and F. R. Harnden, Jr. The structure and evolution of X-ray clusters. *The Astrophysical Journal*, 234: L21–L25, November 1979.

H. Kang, D. Ryu, R. Cen, and D. Song. Shock-heated Gas in the Large-Scale Structure of the Universe. *The Astrophysical Journal*, 620:21–30, February 2005.

H. Karttunen. *Fundamental astronomy*. Physics and Astronomy Online Library. Springer, 2003.

J. Kemmer and G. Lutz. New detector concepts. *Nuclear Instruments and Methods in Physics Research A*, 253:365–377, January 1987.

J. Kemmer, G. Lutz, U. Prechtel, K. Schuster, M. Sterzik, L. Strüder, and T. Ziemann. Experimental confirmation of a new semiconductor detector principle. *Nuclear Instruments and Methods in Physics Research A*, 288:92–98, March 1990.

E. J. Kennedy, G. T. Alley, C. L. Britton, P. L. Skubic, B. Gray, and A. Wu. Radiation effects on JFETS, MOSFETS, and bipolar transistors, as related to SSC circuit design. *Nuclear Instruments and Methods in Physics Research A*, 307:452–457, October 1991.

R. Kippenhahn and A. Weigert. *Stellar structure and evolution*. Astronomy and astrophysics library. Springer-Verlag, 1994.

G.F. Knoll. *Radiation detection and measurement*. Wiley, 1979.

P. Lechner, F. Aschauer, L. Bombelli, C. Fiorini, S. Herrmann, T. Lauf, G. Lutz, P. Majewski, A. Meuris, M. Porro, J. Reiffers, R. Richter, A. Stefanescu, L. Strüder, J. Treis, and G. de Vita. The IXO wide-field imager. In *Society of Photo-Optical Instrumentation Engineers (SPIE) Conference Series*, volume 7742 of *Presented at the Society of Photo-Optical Instrumentation Engineers (SPIE) Conference*, July 2010.

M. Livio, G. I. Ogilvie, and J. E. Pringle. Extracting Energy from Black Holes: The Relative Importance of the Blandford-Znajek Mechanism. *The Astrophysical Journal*, 512:100–104, February 1999.

M.S. Longair. *High Energy Astrophysics: Particles, photons and their detection*. High Energy Astrophysics. Cambridge University Press, 1994a.

M.S. Longair. *High Energy Astrophysics: Stars, the galaxy and the interstellar medium*. High Energy Astrophysics. Cambridge University Press, 1994b.

G. Lutz. *Semiconductor radiation detectors: device physics*. Accelerator Physics. Springer, 1999.

G. Lutz, W. Buttler, H. Bergmann, P. Holl, B. J. Hosticka, P. F. Manfredi, and G. Zimmer. Low noise monolithic CMOS front end electronics. *Nuclear Instruments and Methods in Physics Research A*, 263:163–173, January 1988.

Daniel Maier. Aufbau eines science verification models fr die simbol-x mission. *diploma thesis*, 2009.

Michael Martin. Development of high throughput x-ray instrumentation for fast timing studies. *dissertation*, 2009.

N. Meidinger, R. Andritschke, S. Ebermayer, J. Elbs, O. Hälker, R. Hartmann, S. Herrmann, N. Kimmel, G. Schächner, F. Schopper, H. Soltau, L. Strüder, and G. Weidenspointner. Development of the focal plane PNCCD camera system for the X-ray space telescope eROSITA. *Nuclear Instruments and Methods in Physics Research A*, 624:321–329, December 2010.

I. Morison. *Introduction to Astronomy and Cosmology*. Wiley, 2008.

S. S. Murray, J. H. Chappell, M. S. Elvis, W. R. Forman, and J. E. Grindlay. The AXAF high resolution camera (HRC) and its use for observations of distant clusters of galaxies. *Astrophysical Letters Communications*, 26:113–125, 1987.

I. Negueruela. On the nature of Be/X-ray binaries. *Astronomy and Astrophysics*, 338:505–510, October 1998.

J. A. Nousek, G. P. Garmire, G. R. Ricker, S. A. Collins, and G. R. Reigler. The AXAF CCD Imaging Spectrometer Experiment (ACIS). *Astrophysical Letters Communications*, 26:35–41, 1987.

J. R. Oppenheimer and G. M. Volkoff. On Massive Neutron Cores. *Physical Review*, 55:374–381, February 1939.

F. Özel, T. Güver, and D. Psaltis. The Mass and Radius of the Neutron Star in EXO 1745-248. *The Astrophysical Journal*, 693:1775–1779, March 2009.

L. E. Peterson. Instrumental technique in X-ray astronomy. *Instrumental Technique in X-ray Astronomy*, 13:423–509, 1975.

M. Porro, C. Fiorini, and L. Strüder. Theoretical comparison between two different filtering techniques suitable for the VLSI spectroscopic amplifier ROTOR. *Nuclear Instruments and Methods in Physics Research A*, 512:179–190, October 2003.

M. Porro, G. de Vita, S. Herrmann, T. Lauf, J. Treis, A. Wassatsch, L. Bombelli, and C. Fiorini. ASTEROID: A 64 channel ASIC for source follower readout of DEPFET arrays for X-ray astronomy. *Nuclear Instruments and Methods in Physics Research A*, 617:351–357, May 2010.

S. Rosswog and M. Brüggen. *Introduction to high-energy astrophysics*. Cambridge University Press, 2007.

C. Sandow, L. Andricek, P. Fischer, R. Kohrs, H. Krüger, G. Lutz, H. G. Moser, L. Reuen, R. H. Richter, L. Strüder, J. Treis, M. Trimpl, and N. Wermes. Clear-performance of linear DEPFET devices. *Nuclear Instruments and Methods in Physics Research A*, 568:176–180, November 2006.

G. Schächner, R. Andritschke, O. Hälker, S. Herrmann, N. Kimmel, N. Meidinger, and L. Strüder. First qualification and selection of the eROSITA PNCCDs. *Nuclear Instruments and Methods in Physics Research A*, 624:330–333, December 2010.

P. Schneider. *Extragalactic astronomy and cosmology: an introduction*. Springer, 2006.

E. J. Schreier, P. Gorenstein, and E. D. Feigelson. High-resolution X-ray observations of M87 - Nucleus, jet and radio halo. *The Astrophysical Journal*, 261:42–50, October 1982.

H. Spieler. *Semiconductor detector systems*. Series on semiconductor science and technology. Oxford University Press, 2005.

A. Stefanescu, M. W. Bautz, D. N. Burrows, L. Bombelli, C. Fiorini, G. Fraser, K. Heinzinger, S. Herrmann, M. Kuster, T. Lauf, P. Lechner, G. Lutz, P. Majewski, A. Meuris, S. S. Murray, M. Porro, R. Richter, A. Santangelo, G. Schaller, M. Schnecke, F. Schopper, H. Soltau, L. Strüder, J. Treis, H. Tsunemi, G. de Vita, and J. Wilms. The Wide Field Imager of the International X-ray Observatory. *Nuclear Instruments and Methods in Physics Research A*, 624:533–539, December 2010.

L. Strüder, U. Briel, K. Dennerl, R. Hartmann, E. Kendziorra, N. Meidinger, E. Pfeffermann, C. Reppin, B. Aschenbach, W. Bornemann, H. Bräuninger, W. Burkert, M. Elender, M. Freyberg, F. Haberl, G. Hartner, F. Heuschmann, H. Hippmann, E. Kastelic, S. Kemmer, G. Kettenring, W. Kink, N. Krause, S. Müller, A. Oppitz, W. Pietsch, M. Popp, P. Predehl, A. Read, K. H. Stephan, D. Stötter, J. Trümper, P. Holl, J. Kemmer, H. Soltau, R. Stötter, U. Weber, U. Weichert, C. von Zanthier, D. Carathanassis, G. Lutz, R. H. Richter, P. Solc, H. Böttcher, M. Kuster, R. Staubert, A. Abbey, A. Holland, M. Turner, M. Balasini, G. F. Bignami, N. La Palombara, G. Villa, W. Buttler, F. Gianini, R. Lainé, D. Lumb, and P. Dhez. The European Photon Imaging Camera on XMM-Newton: The pn-CCD camera. *Astronomy and Astropysics*, 365:L18–L26, January 2001.

U. Tietze and C. Schenk. *Halbleiter-schaltungstechnik:*. Springer, 2002.

J. Treis, P. Fischer, O. Hälker, M. Harter, S. Herrmann, R. Kohrs, H. Krüger, P. Lechner, G. Lutz, I. Peric, M. Porro, R. H. Richter, L. Strüder, M. Trimpl, and N. Wermes. First results of DEPFET-based active-pixel-sensor prototypes for the XEUS wide-field imager. In A. D. Holland, editor, *Society of Photo-Optical Instrumentation Engineers (SPIE) Conference Series*, volume 5501 of *Presented at the Society of Photo-Optical Instrumentation Engineers (SPIE) Conference*, pages 89–100, September 2004.

J. Treis, P. Fischer, O. Hälker, M. Harter, S. Herrmann, R. Kohrs, H. Krüger, P. Lechner, G. Lutz, I. Peric, M. Porro, R. H. Richter, L. Strüder, M. Trimpl, and N. Wermes. Study of noise and spectroscopic performance of DEPMOSFET matrix prototypes for XEUS. *Nuclear Instruments and Methods in Physics Research A*, 568:191–200, November 2006.

A. Treves and M. Colpi. The observability of old isolated neutron stars. *Astronomy and Astropysics*, 241:107–111, January 1991.

J. Truemper, W. Pietsch, C. Reppin, W. Voges, R. Staubert, and E. Kendziorra. Evidence for strong cyclotron line emission in the hard X-ray spectrum of Hercules X-1. *Astrophysical Journal*, 219:L105–L110, February 1978.

M. J. L. Turner, A. Abbey, M. Arnaud, M. Balasini, M. Barbera, E. Belsole, P. J. Bennie, J. P. Bernard, G. F. Bignami, M. Boer, U. Briel, I. Butler, C. Cara,

C. Chabaud, R. Cole, A. Collura, M. Conte, A. Cros, M. Denby, P. Dhez, G. Di Coco, J. Dowson, P. Ferrando, S. Ghizzardi, F. Gianotti, C. V. Goodall, L. Gretton, R. G. Griffiths, O. Hainaut, J. F. Hochedez, A. D. Holland, E. Jourdain, E. Kendziorra, A. Lagostina, R. Laine, N. La Palombara, M. Lortholary, D. Lumb, P. Marty, S. Molendi, C. Pigot, E. Poindron, K. A. Pounds, J. N. Reeves, C. Reppin, R. Rothenflug, P. Salvetat, J. L. Sauvageot, D. Schmitt, S. Sembay, A. D. T. Short, J. Spragg, J. Stephen, L. Strüder, A. Tiengo, M. Trifoglio, J. Trümper, S. Vercellone, L. Vigroux, G. Villa, M. J. Ward, S. Whitehead, and E. Zonca. The European Photon Imaging Camera on XMM-Newton: The MOS cameras : The MOS cameras. *Astronomy and Astropysics*, 365:L27–L35, January 2001.

A. Unsöld and B. Baschek. *Der neue Kosmos: Einführung in die Astronomie und Astrophysik*. Springer, 2002.

A. Weigert, H.J. Wendker, and L. Wisotzki. *Astronomie und Astrophysik: Ein Grundkurs*. Wiley VCH Verlag GmbH, 2009.

M. C. Weisskopf, H. D. Tananbaum, L. P. Van Speybroeck, and S. L. O'Dell. Chandra X-ray Observatory (CXO): overview. In J. E. Truemper & B. Aschenbach, editor, *Society of Photo-Optical Instrumentation Engineers (SPIE) Conference Series*, volume 4012 of *Presented at the Society of Photo-Optical Instrumentation Engineers (SPIE) Conference*, pages 2–16, July 2000.

H. Wolter. Spiegelsysteme streifenden Einfalls als abbildende Optiken für Röntgenstrahlen. *Annalen der Physik*, 445:94–114, 1952. doi: 10.1002/andp.19524450108.

K. S. Wood, J. F. Meekins, D. J. Yentis, H. W. Smathers, D. P. McNutt, R. D. Bleach, H. Friedman, E. T. Byram, T. A. Chubb, and M. Meidav. The HEAO A-1 X-ray source catalog. *The Astrophysical Journal*, 56:507–649, December 1984.

Danksagung

Ich möchte mich ganz herzlich bei all denen bedanken, die mich während der Diplomarbeit unterstützt haben. Was die Arbeit an der Diplomarbeit selbst betrifft, gilt besonderer Dank Daniel Maier, Christoph Tenzer, Jürgen Dick, Henning Wende, Thomas Schanz, Giuseppe Distratis und meinem Professor Andrea Santangelo.

Für erfolgreiches Ablenken und eine gute Zeit möchte ich mich außerdem bei meiner Familie und Freunden bedanken.

DANKE!

Plagiatserklärung

Hiermit erkläre ich, dass zur Erstellung dieser Diplomarbeit keine als die angegebenen Quellen und Hilfsmittel verwendet wurden.

Ort, Datum Unterschrift